Stony Brook University

Rayleigh-Taylor Turbulent Mixing Simulations

A Dissertation Presented

by

Tulin Kaman

to

The Graduate School

in Partial Fulfillment of the

Requirements

for the Degree of

Doctor of Philosophy

in

Applied Mathematics and Statistics

Stony Brook University

August 2012

Stony Brook University

The Graduate School

Tulin Kaman

We, the dissertation committee for the above candidate for the
Doctor of Philosophy degree, hereby recommend
acceptance of this dissertation.

James Glimm - Dissertation Advisor
Professor, Department of Applied Mathematics and Statistics

Roman Samulyak - Chairperson of Defense
Associate Professor, Department of Applied Mathematics and Statistics

Xiangmin Jiao - Member
Associate Professor, Department of Applied Mathematics and Statistics

Alan Calder - Outside Member
Assistant Professor, Department of Physics and Astronomy

This dissertation is accepted by the Graduate School.

Charles Taber
Interim Dean of the Graduate School

Abstract of the Dissertation

Rayleigh-Taylor Turbulent Mixing Simulations

by

Tulin Kaman

Doctor of Philosophy

in

Applied Mathematics and Statistics

Stony Brook University

2012

We study the Rayleigh-Taylor mixing layer, presenting on simulations in agreement with experimental data. This problem is an idealized subproblem of important scientific and engineering problems, for example the gravitationally induced mixing in oceanography and performance assessment for inertial confinement fusion. Engineering codes commonly achieve correct simulations through the calibration of adjustable parameters. In this sense, they are interpolative and not predictive. As computational science moves from the interpolative to the predictive and reduces the reliance on experiment the quality of decision making improves. The diagnosis of errors in a multiparameter, multiphysics setting is daunting, so we address this issue in the proposed idealized

setting. The validation tests presented are then a test for engineering codes, when used for complex problems containing Rayleigh-Taylor features.

The Rayleigh-Taylor growth rate, characterized by a dimensionless but non-universal parameter α, describes the outer edge of the mixing zone. Increasingly accurate Front Tracking/LES simulations reveal non-universality of the growth rate and agreement with experimental data. Increased mesh resolution allows reduction in the role of key subgrid models.

We study the effect of long wavelength perturbations on the mixing growth rate. A self-similar power law for the initial perturbation amplitudes is here inferred from experimental data. We show a maximum $\pm 5\%$ effect on the growth rate. Large (factors of 2) effects, as predicted in some models and many simulations, are inconsistent with experimental data of Youngs and co-authors. The inconsistency of the model lies in the treatment of the dynamics of the bubbles, which are the shortest wavelength modes for this problem. An alternate theory for this shortest wavelength, based on the bubble merger model, was previously shown to be consistent with experimental data. Turbulent mixing at the molecular level and turbulent combustion are remaining challenges for turbulent mixing studies.

Theoretical studies suggest that convergence of numerical solutions, considered within an LES regime, is to a space time dependent probability distributions (Young measures). This point of view is proposed for the study of micro-observables, which describe the molecular mixing rate. New results comparing our simulations to experimentally observed molecular mixing rates are reported.

Key Words: Front Tracking, Large Eddy Simulation, Subgrid Scale Model, Turbulent Mixing, Uncertainty Quantification

To my parents
Salime Kaman & Nevzat Kaman

Table of Contents

List of Figures

List of Tables

Acknowledgements

I would like to express my sincere gratitude to my advisor, Professor James Glimm, for his continuous support of my Ph.D study. It has been honor and privilage to have worked under the direction of Professor James Glimm. Through his guidance, I have grown as a student and became an applied mathematician who has knowledge in mathematics, physics, and computer science. He helps me to have much better understanding in everything. He gives me the courage to develop and express myself professionally. That makes me grown as a student, accomplish a lot during my graduate study years. He is a lifetime role model for me.

I am deeply indebted to the support of Professor David H. Sharp, Professor Xiaolin Li, Roman Samulyak and Xiangmin Jiao from whom I have learned many important scientific and mathematical skills; Dr. Sameer Shende and Dr. Vitali Morozov from whom I have learned high performance computing skills. I would like to thank Professor Alan Calder for being on my dissertation committee. It is a pleasure to thank David Youngs for helpful comments and for providing unpublished information related to his experiments.

I would like to thank all my friends during my years of study as a graduate student at Stony Brook for their friendship and encouragement. In particular,

I would like to mention So-Youn Shin, Eunah Li, Wurigen Bo, Justin Iwerks, Ryan Kaufman, Bryan Clark, JoungDong Kim and HyunKyung Lim.

The continued support of my family has motivated me throughout my academic career. Their love, support and encouragement have given me the strength to achieve my goals. I would like to thank to my sister, Pelin and my parents, Salime and Nevzat Kaman. My dissertation is dedicated to them.

Chapter 1

Introduction

1.1 Overview and Motivation

Turbulent mixing is a long standing problem. We consider the Rayleigh-Taylor (RT) mixing problem [6, 52], in which a light fluid accelerates a heavy fluid. Numerical efforts to solve this problem date over 60 years, and only recently have systematic numerical solutions based on compressible fluid dynamics been found that address an experimental range of fluid parameters for both immiscible and miscible fluids, the latter over a range of Schmidt numbers [35, 36, 41, 13]. The problem is to predict the growth rate α, defined in terms of the penetration distance h of the light fluid into the heavy fluid via the equation

$$h = \alpha A g t^2 \ , \tag{1.1}$$

where $A = (\rho_2 - \rho_1)/(\rho_2 + \rho_1)$ is the Atwood ratio, a dimensionless measure of the density contrast, and g is the acceleration, applied normal to an interface separating fluids of density ρ_1 and ρ_2.

The scope of this study is the status of numerical simulations and theoretical models to determine α in the regime of laboratory experiments, and the comparison of simulation and theory to experiment in this regime.

As documented below, these simulations show agreement with experiment. An additional of simulation [44], based on an incompressible code, shows agreement with experiment for moderate Schmidt numbers. We also mention our earlier simulations, for example [14], stretching over a number of years, with increasing agreement to experiment, and we mention the particle based simulation, with mixing rates within the experimental range [27]. These simulations are parameter free in their agreement with experiment.

To discuss validation, we first introduce a definition. Validation of a simulation refers to comparison of a simulation to an experiment, with a small error [1]. Of course the issues of the size of the error, the range of distinct experiments for which agreement is obtained and the type of measurements used for which approximate agreement is reported are then open issues. For such reasons, validation is seldom complete. We do exclude simulations with adjustable parameters for which the parameter fitting experiments and the validation checking experiments are not independent.

Other simulations [55, 3] show agreement with experiment, but make use of an adjustable parameter (the magnitude of an assumed long wavelength perturbation in the initial data). Agreement is achieved by selection of a suitable value for this parameter. Since the class of experiments (with a relatively common α) used to adjust this parameter coincides with the data being used for comparison to experiment, such simulations do not meet the requirements

of validation. Many simulations (see for example [11]) disagree with experiment in their values of α by factors of 2 or more, a fact commonly attributed [55, 10, 3] to unmeasured long wavelength perturbations in the initial conditions.

Questions have been raised regarding our validation studies, a particularly interesting issue in view of the above noted simulation-experiment discrepancy for many codes.

The three issues which have been raised are

1. Long wavelength perturbations could be present in the initial data, and could contribute to the self-similar growth constant α by a factor of two or more.

2. Simulations that depend on subgrid models leave open the validity of the subgrid models.

3. Some workers have conjectured the existence of a "true" self-similar regime, universal relative to fluid transport parameters, which may be distinct from regimes of laboratory experiments.

Item 2 appears to be at most marginally credible, in view of

- the 20 year history of validated turbulence computations using dynamic subgrid scale (SGS) models of the type considered here by a large community of computational scientists and engineers and for a wide range of problems,

- our own multiple validated RT simulations with a maximum 6% and usually 0% discrepancy (relative distance outside of reported error bounds) with experiment, including examples with measured initial conditions used in the simulation, in contrast to many non validated RT simulations using compressible hydro codes with a typical factor of two discrepancy to experimental data.

- the highly resolved simulation shown in Fig. 6.1 below, with full resolution of the critical Weber length scale for droplet breakup, shows agreement with experimental data and convergence under mesh refinement. Additional mesh convergence studies are presented in [35, 36].

Item 1 is addressed here, as the main purpose of this thesis. Central to the Item 1 claims addressed here is the assertion that long wavelength initial perturbations account for a factor of two or more in α in the regime of laboratory experiments and that in the absence of such perturbations, simulation results with $\alpha \approx 0.02$ or 0.03 are correct.

Our main conclusions regarding long wavelength perturbations are

1a Multiple simulations achieve αs in highly accurate agreement with experiment. The αs are not universal, but depend on specific experimental parameters. The simulations have sufficient accuracy to resolve these differences. A number of parameters showing α sensitivity are identified.

1b Initial data can be reconstructed for the Smeeton-Youngs rocket rig data.

1c Even with generous error margins for the reconstruction, the resulting uncertainty in α is $\pm 5\%$.

1d The Smeeton-Youngs experiments have significantly weak initial long wave perturbation strength.

1e The long wave perturbations as measured for the water channel experiments are sufficient to explain perhaps a 30% change in the value of α but do not explain a change by a factor of 2.

1f The theoretical model [10] for bubble dynamics appears to be less suited to describe experimental data than is the bubble merger model [21, 8]. We also mention the bubble merger model [2, 25, 51] which correctly predicts the mixing growth rate α, but in contrast to the [8], incorrectly predicts the experimental values of the bubble height to width ratio.

Items 1b, 1c, 1d, and 1f are newly reported here.

New results presented here include new simulation studies for [54] immiscible experiment #105, the analysis and inference of initial conditions, the error bounds and uncertainty analysis for these initial conditions and the prediction of α for this experiment. We also study the convergence under mesh refinement of the second moments for species concentration and velocities, quantities of interest in a miscible experiment #112 [54].

1.2 Front Tracking and Large Eddy Simulations

The essential features of the algorithms used here are front tracking, to achieve resolution of steep and sharp density gradients, and large eddy simulations (LES) with subgrid scale (SGS) terms to model the diffusive transport corrections to the mesh (Reynolds) averaged Navier-Stokes equations (Chapter 2 Sec.2.1). These features are included in the multipurpose simulation code FronTier, as we now describe.

1.2.1 Front Tracking Methods

An important part of our algorithm is the use of front tracking, to control numerical mass and thermal diffusion and to allow accurate modeling of sharp interface surface tension forces, laminar and turbulent mass and thermal diffusion. This algorithm has been subject to an extensive verification (mesh convergence) study and comparison to a simple theoretical model [39] in addition to the validation tests mentioned above.

Front Tracking assigns computational degrees to a surface, or interface, moving freely through an Eulerian grid. The discretization of the Eulerian grid variables is conventional, using the MUSCL algorithm [9], with the exception that for stencils cut by the front, extrapolated ghost cell values are used to complete the stencil so that it contains states from a single side of the interface. The front variables acquire a velocity field via a two-sided interpolation of states from the interior, projected onto a single normal velocity field through solution of a Riemann problem [4]. The front is the location of

a sharp discontinuity in fluid properties, in the case of immiscible fluids, and it is an iso-concentration contour in the case of miscible fluids with a steep concentration gradient.

It is well known that Eulerian advection schemes suffer from significant levels of numerical mass diffusion, in the case of a steep concentration gradient advected by the fluid relative to a grid. Lagrangian methods can be used to mitigate this problem, but they suffer from mesh distortion and remeshing interpolation errors when taken to complex interfaces at late time. Volume of fluids methods [49, 50] provide a reconstruction of the interface, in order to overcome these problems. Level sets, in which the level set distance to the interface is advected have also been used to mitigate Eulerian mass diffusion problems. The ghost cell extrapolation idea, at the heart of the level set approach, is based on the same idea, part of the original Front Tracking algorithm [20]. Level sets come in several different versions, the simplest of which are of too low a quality to be very useful and the more complicated of which offer little advantage in regard to simplicity over front tracking. A comparison study [12] found Front Tracking to be of higher resolution than either Volume of Fluids or Level Sets.

The front tracking method is an adaptive computational method that provides sharp resolution of a wave front by tracking the interfaces between distinct materials. It represents interfaces explicitly as lower dimensional meshes moving through a rectangular grid. In 2D, the wave is represented by a curve which is comprised of connected line segments. In 3D, the wave is represented by a triangulated mesh. The states (density, pressure and velocity) of fluids

are located in the centers of each grid cell [18, 16, 17]. The method has been implemented in the code *FronTier*.

FronTier solves the equations with the following main steps:

1. interface propagation.

2. interpolation reconstruction.

3. interior states update.

In the interface propagation step, the speed for each interface point is solved by either a local Riemann problem or an interpolation method. Then, a new position for the point is determined from the equation

$$\mathbf{x}^{\text{new}} = \mathbf{x}^{\text{old}} + V\Delta t\mathbf{n} \ , \tag{1.2}$$

where V is the wave speed, $\mathbf{n}$ is the direction normal to the interface at the point and Δt is the time step size.

After all points in the interface are propagated, we get a new interface at a new time level. Methods are implemented in *FronTier* to resolve the topologic change and to optimize all triangles in the interface. In the interpolation reconstruction step, the components (defined in the sense of point set topology relative to the ambient space with the interface removed) at the cell center of all interior points are determined from the propagated interface. In the interior state update step, a Strang splitting is applied and three 1D equations are solved consecutively. All the states on cell centers are updated by a Monotone Upstream-centered Schemes for Conservation Laws (MUSCL scheme). If the

stencil of the scheme does not cross any interface, the states in the stencil are given by the cell center values. Otherwise, a ghost cell method [19] is used to fill the states on the points on the other side of the interface.

FronTier is parallelized with a tensor product domain decomposition. MPI is used to pass states and interface data from one processor to another. FronTier has adopted object oriented programming. Many major functionalities have been modulized to allow users to call them with a minimum knowledge of internal operation and coding.

1.2.2 Large Eddy Simulations/ Subgrid Scale Models

The Navier-Stokes equations solved are the filtered continuity, momentum, energy and concentration equations for two miscible fluid species in an inertial frame. The LES/SGS algorithm is classical [15, 43, 42]. The salient point here is that the LES/SGS algorithm assumes a functional form for the turbulent transport terms, basically of a gradient diffusion nature, but the coefficient of this term, a potentially troublesome free parameter, is actually constrained and determined from the simulation itself. The derivation of the Reynolds averaged equations and the SGS terms with the dynamically determined (parameter free) transport terms is too detailed, with formulas too lengthy to be summarized here, but the reference [42] is an excellent self contained source for this material. The extra equation needed and used to determine the turbulent transport coefficients dynamically comes from looking at two adjacent grid levels, the current grid and a once coarsened grid. On the once coarsened grid, the missing terms and coefficients can be determined in

two ways, leading to a dynamic equation for their determination. Assuming an asymptotic relation, the coefficient on the once coarser mesh determines the coefficient on the current mesh. The combination of these two algorithms appears to be very powerful in its ability to overcome difficulties which have impeded progress in a variety of turbulent mixing problems, and for a variety of researchers.

All simulations reviewed here are in 3D. The sides of the computational domain (parallel to the direction of the gravitational field g) are periodic; the top and bottom are no flow boundaries.

1.3 Dissertation Organization

Chapter 1 first gives the overview and brief review of the front tracking, Large Eddy Simulations, Subgrid Scale Model. The multi-species compressible Navier-Stokes equation, filtered at a grid level are given in Chapter 2. In Chapter 3, five immiscible experiments being considered here are analyzed. We have quantified the allowed long wavelength perturbation amplitudes, by an analysis of the recorded early time data in Chapter 4. We compare superposition and bubble merger velocities to the actual bubble front velocity in Chapter 5. In Chapter 6, we show the convergence under mesh refinement of the second moments for species concentration and velocities, quantities of interest in a miscible Rayleigh-Taylor experiment #102 [54]. The conclusion is discussed in Chapter 7.

Chapter 2

Front Tracking RT Simulations

Simulations in agreement with 14 experiments were previously reported [35, 36, 41, 13], see Table 2.1. We return to two of these experiments with new simulation and data analysis (UQ) results.

We return to experiment #105 of [54] and achieve agreement with experiment, and with simulations going through all data points. See Table 2.1. Simulations I, II, III presented in Chapter 6 Fig. 6.1 and related to uncertainty quantification for the initial conditions are new. Simulation III has a much finer grid, of 111μ, sufficient to fully resolve the Weber length scale associated with droplet breakup, the dominant physics for the immiscible mixing of this experiment. The initial conditions of simulation III are the best estimate reconstruction of the initial conditions from the measured data. The agreement among the three simulations and these with experiment is sufficient to assert the mesh convergence and approximate mesh independence of the results. Further mesh convergence studies were reported in [35, 36].

Table 2.1: Comparison of FT simulation to experiment. * Original simulation results presented here. † Simulation and experimental results reported with two significant digits only. Discrepancy refers to the comparison of results outside of uncertainty intervals, if any, as reported.

Ref.	Exp.	Sim. Ref.	α_{exp}	α_{sim}	Discrepancy †
[54]	#112	*[35]	0.052	0.055	6%
[54]	#105	*	0.072	0.076 ± 0.004	0%
[54, 48]	10 exp.	[13]	0.055-0.077	0.066	0%
[47]	air-He	[41]	0.065-0.07	0.069	0%
[46]	Hot-cold	[35, 22]	0.070 ± 0.011	0.075	0%
[46]	Salt-fresh	[22]	0.085 ± 0.005	0.084	0%

2.1 The Navier-Stokes Equations

The Navier-Stokes equations solved are the filtered continuity, momentum, energy and concentration equations for two miscible fluid species in an inertial frame, as written in Eqs.(2.1-2.4). The filtered quantities are considered to be mesh block averages, and denoted with an overbar, while mass averaged quantities are denoted with a tilde. Repeated indices are summed.

$$\frac{\partial \overline{\rho}}{\partial t} + \frac{\partial \overline{\rho}\widetilde{v_i}}{\partial x_i} = 0 \ , \tag{2.1}$$

$$\frac{\partial \overline{\rho}\widetilde{v_j}}{\partial t} + \frac{\partial (\overline{\rho}\widetilde{v_i}\widetilde{v_j} + \overline{p}\delta_{ij})}{\partial x_i} = \frac{\partial \overline{d_{ij}}}{\partial x_i} - \frac{\partial \tau_{ij}}{\partial x_i} \ , \tag{2.2}$$

$$\begin{aligned} \frac{\partial \overline{E}}{\partial t} + \frac{\partial (\overline{E} + \overline{p})\widetilde{v_i}}{\partial x_i} \ &= \frac{\partial \overline{d_{ij}}\widetilde{v_j}}{\partial x_i} + \frac{\partial}{\partial x_i}\left(\overline{\kappa}\frac{\partial \widetilde{T}}{\partial x_i}\right) + \frac{\partial}{\partial x_i}\left((\widetilde{H_h} - \widetilde{H_l})\overline{\rho}\widetilde{D}\frac{\partial \widetilde{\psi}}{\partial x_i}\right) \\ &+ \left(\frac{1}{2}\frac{\partial \tau_{kk}\widetilde{v_i}}{\partial x_i} - \frac{\partial q_i^{(H)}}{\partial x_i} - \frac{\partial q_i^{(T)}}{\partial x_i} - \frac{\partial q_i^{(V)}}{\partial x_i}\right) \ , \end{aligned} \tag{2.3}$$

$$\frac{\partial \overline{\rho}\widetilde{\psi}}{\partial t} + \frac{\partial \overline{\rho}\widetilde{\psi}\widetilde{v_i}}{\partial x_i} = \frac{\partial}{\partial x_i}\left(\overline{\rho}\widetilde{D}\frac{\partial \widetilde{\psi}}{\partial x_i}\right) - \frac{\partial q_i^{(\psi)}}{\partial x_i} \ , \tag{2.4}$$

where the SGS variables, τ_{ij}, $q_i^{(H)}$, $q_i^{(T)}$, $q_i^{(V)}$ and $q_i^{(\psi)}$, are expressed as

$$\tau_{ij} = \overline{\rho}(\widetilde{v_i v_j} - \widetilde{v_i}\widetilde{v_j}) \tag{2.5}$$

$$q_i^{(H)} = \overline{\rho}(\widetilde{c_p T v_i} - \widetilde{c_p}\widetilde{T}\widetilde{v_i}) \tag{2.6}$$

$$q_i^{(T)} = \frac{1}{2}\overline{\rho}(\widetilde{v_k v_k v_i} - \widetilde{v_k}\widetilde{v_k}\widetilde{v_i}) \tag{2.7}$$

$$q_i^{(V)} = \overline{d_{ij} v_j} - \overline{d_{ij}}\widetilde{v_j} \tag{2.8}$$

$$q_i^{(\psi)} = \overline{\rho}(\widetilde{\psi v_i} - \widetilde{\psi}\widetilde{v_i}) \ . \tag{2.9}$$

The viscous stress tensor, d_{ij}, in momentum and energy equations is expressed as

$$\overline{d_{ij}} = \overline{\nu_d}\left(\left(\frac{\partial \widetilde{v_i}}{\partial x_j} + \frac{\partial \widetilde{v_j}}{\partial x_i}\right) - \frac{2}{3}\frac{\partial \widetilde{v_k}}{\partial x_k}\delta_{ij}\right) \ , \tag{2.10}$$

where $\overline{\nu_d} = \overline{\rho\nu_k}$ is the filtered dynamic viscosity. In Eq.(2.3), $\widetilde{H_h}$ and $\widetilde{H_l}$ are the partial specific enthalpy of each species defined by

$$\widetilde{H_h} = \widetilde{e_h} + \frac{\overline{p}}{\overline{\rho}} \tag{2.11}$$

$$\widetilde{H_l} = \widetilde{e_l} + \frac{\overline{p}}{\overline{\rho}} \ , \tag{2.12}$$

where $\widetilde{e_h}$ and $\widetilde{e_l}$ are the specific internal energy of each species.

Chapter 3

The Experiments

We consider five immiscible experiments, #56, #63 [5] and #104, #105, #114 [54]. Immiscible experiments were selected as we analyze amplitudes of individual bubbles and these are more sharply defined in the experimental record than are the bubbles in the miscible experiments. These five experiments were selected on the basis of sufficient supporting data in the experimental reports. We chose #105 for numerical simulations as it had the lowest Atwood number, making it less costly to simulate with a compressible explicit algorithm. Of the five experiments, one (#63) was deliberately vibrated to create a low amplitude standing wave as part of the initial conditions. This experiment has a clearly defined large central bubble, distinct from the statistical ensemble of bubbles around it. One (#104), according to the comments in the experimental report, has mode 2 perturbations initially. One (#56) has, according to our own observations, a possible long wavelength perturbation in its early time steps. Two (#105 and #114) show no visual signs or experimentally reported indications of long wavelength perturbations. There seems

to be no correlation between the observations of long wave perturbations or their absence and the values observed for α. The two experiments nominally free of such perturbations have the largest value of α (#105: $\alpha = 0.072$) and the next to smallest value of α (#114: $\alpha = 0.060$) of the five.

In view of this experimental record, there appears to be no basis for concluding that run to run variations in the long wavelength perturbations explain experimental variability of $\pm 10\%$ in α. An assertion that a factor of 2 to 3 modification in α can result from long wavelength perturbations in the experimental data seems still less plausible. With the two significant digit accuracy (or, more realistically the agreement within 10%, in the absence of experimental error bars) of our simulations in comparison to experiment, it would seem that the experimental variability in α will be explained in some other aspect of the experiments.

The methods in Chapter 4 are applicable to all immiscible experiments from [54], and the resulting UQ bounds for α could be inferred to apply to the immiscible experiments as well, as the long wavelength initial perturbations (estimated in this analysis) should be a function of the experimental method and independent of the miscibility or immiscibility of the fluids. To illustrate the available data, we reproduce (with permission) the experimental plates from experiment #105 in Figs. 3.1-3.3.

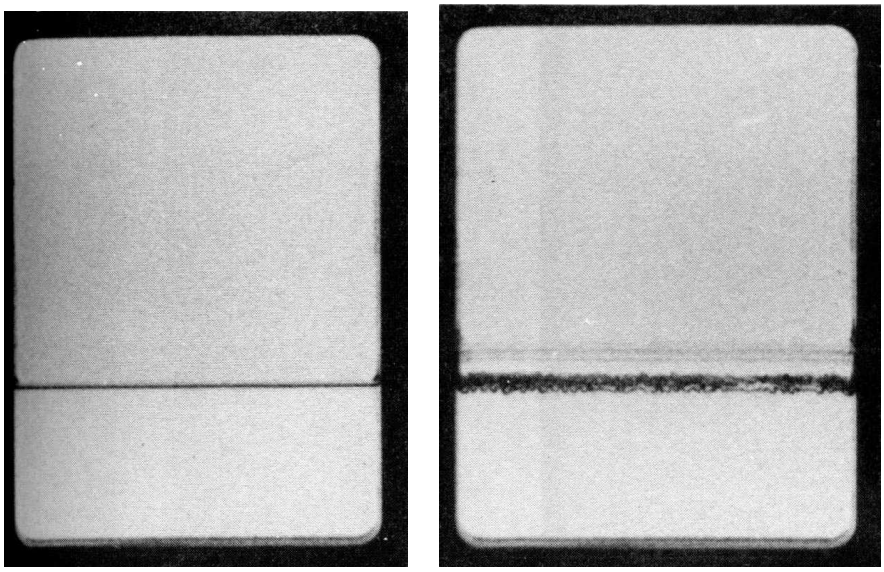

Figure 3.1: First experimental plate (left), second experimental plate (right) for experiment #105. (c) British Crown Copyright 2010/MOD. Experimental figure courtesy of D. Youngs.

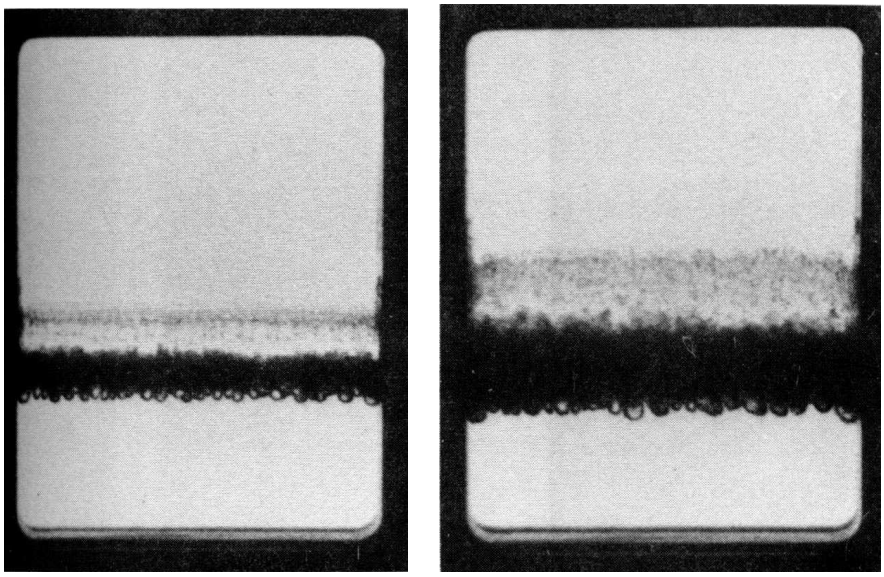

Figure 3.2: Plates 3 and 4. (c) British Crown Copyright 2010/MOD. Experimental figure courtesy of D. Youngs.

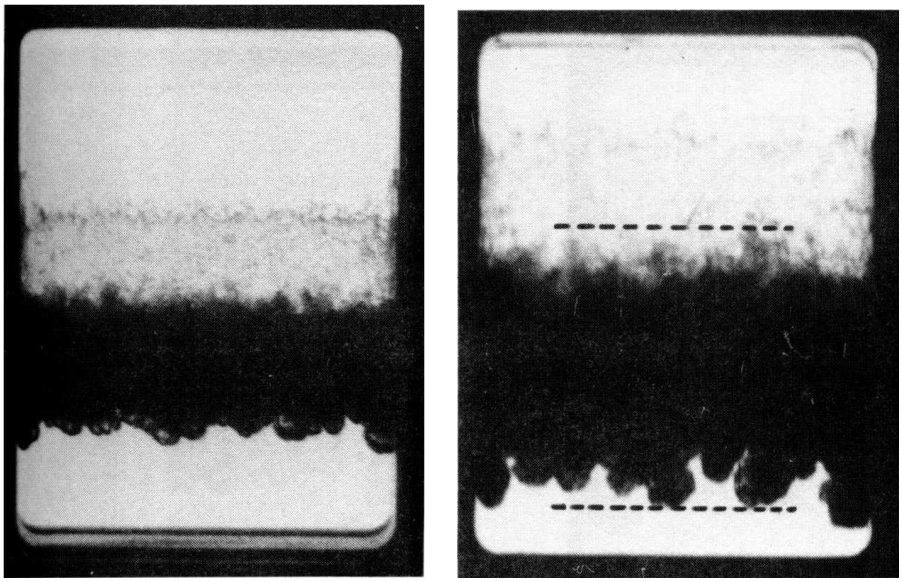

Figure 3.3: Plates 5 and 6. (c) British Crown Copyright 2010/MOD. Experimental figure courtesy of D. Youngs.

Chapter 4

Initial Conditions for Turbulent Mixing Simulations

4.1 Initial Perturbations, α and Numerical Simulations

We present a numerical simulation test that assesses the effects of long wavelength initial perturbations on α. We report here simulations of experiment #105 [54]. According to methods explained in Section 4.3, we reconstruct the $t = 0$ data from early time experimental plates, and through estimates of the errors in this reconstruction explained in Section 4.5 we bound α in a range 0.076 ± 0.004. The experimental $\alpha = 0.072$ falls within this uncertainty quantification simulation interval. The influence of the long wavelength initial perturbations on α is $\leq \pm 5\%$.

The purpose of the reconstruction and the simulation is validation and uncertainty quantification. We use knowledge of the early time and inferred initial data to predict the late time behavior in agreement with experiment. In a validation study, use of experimental data (which is independent of the ob-

served data) is appropriate. The early time spectral amplitudes of the perturbations is independent of the long time growth rate α, other than the fact that the two are linked by solutions of the Navier-Stokes equations. It is precisely this linkage (i.e. the Navier-Stokes equation, solved by a Front Tracking/LES algorithm) which we investigate and validate. For this purpose, the initial or early time data is an input, not an output, and is logically independent of the dynamical and numerical evolution output being validated. This part of our work is a validation result. We assess uncertainties in the reconstruction and carry forward these errors to late time results to assess uncertainty in the late time associated with partial knowledge or partial uncertainty of the long wavelength component of the initial conditions. This is uncertainty quantification. These issues are illustrated in Eq. (4.1), with the left inference diagram representing a classical validation inference (input Plate 1) to output Plate 6) and the right, the validation inference diagram we employ. All arrows represent solution algorithms. The first arrow on the right is backward in time and uses linearized equations and analytical formulas from dispersion relations. (Plate 3 to input Plate 1 to final Plate 6).

$$\text{Plate } 1 \rightarrow \text{Plate } 6 \; ; \quad \text{Plate } 3 \rightarrow \text{Plate } 1 \rightarrow \text{Plate } 6 \tag{4.1}$$

4.2 Modal Analysis of Experimental Data

In the plates, the acceleration is downward, and the inertial force (the effective "gravity") is upward. Thus the light fluid, initially above the heavy, is forced down. The bubbles are elements of light fluid penetrating downward

into the lower, heavy fluid, and are clearly evident in these experimental plates.

After a brief initial time period, the interface separating the two phases cannot be represented as a (single valued) function $z = z(x, y)$. In the experimental plates, only the upper and lower envelopes of the interface are visible, as viewed along the x axis direction, so that the interface envelope is displayed as a function of y alone. Thus an analysis of the interface based on experimental data must start with some simplifications. Following [28, 29], we discard all information other than the sequence of bubble minima at each time. In effect, we are assuming that the bubbles have an equal width and that the height of each bubble minima is sufficient information for the subsequent analysis.

We start by recording the amplitudes of all bubble minima at the times $t = t_j$ of each of the $j = 0, 1, \cdots$ experimental plates. The decision of which local minima to disregard (small minima in the middle of a spike, representing a bubble already lost from the ensemble or closely adjacent bubbles, partially merged, to be counted as one bubble) is partially subjective. As a check, the data acquisition was repeated independently, with only minor differences observed. For example in Table 5.1, the independently read data led to average velocity differences of about 10%, with no significant change in the conclusions.

The minima are taken relative to the experimentally recorded extreme minima, so that parallax issues, addressed in the experimental data analysis, are also addressed in our data analysis. The number $n_{\max}(t)$ of such minima is time dependent, decreasing with time. We regard the amplitudes at the minima as functions on discrete equally spaced locations $x_0, \cdots, x_{n_{\max}-1}$, or conceptually as a function defined on $Z_{n_{\max}}$, the group of integers reduced

modulo $n_{\max}$. A discrete Fourier transform of a function f_j on $Z_{n_{\max}}$ is defined by the formula

$$A(n,t) \equiv \hat{f}_n = \frac{1}{n_{\max}} \sum_{j=0}^{n_{\max}-1} f_j e^{-\frac{2\pi i}{n_{\max}} nj} \qquad n = 0, \cdots, [n_{\max}/2] \ , \tag{4.2}$$

where $[x]$ is the integer part of the real number x. Then (4.2) defines a function on the dual group, which is also $Z_{n_{\max}}$. Because the f_j are real, the $\hat{f}_n$ satisfy an identity $\bar{\hat{f}}_n = \hat{f}_{-n}$, and in the arithmetic of $Z_{n_{\max}}$, $-n = n_{\max} - n$. Accordingly, such modes, above the Nyquist limit, are omitted, as is indicated in (4.2). The complex Fourier series (4.2) gives rise to independent sin and cos modes for the same wave number, so there are $n_{\max}$ real Fourier modes in the series.

Because we are transforming the bubble minima and not the full bubble envelope, the $n = 0$ mode has a special interpretation. As can be seen from Eq. (4.2), the $n = 0$ mode determines the mean bubble penetration height (mean bubble amplitude) at $t = t_j$. The bubbles themselves are the shortest wavelength modes present at $t = t_j$, as is evident from inspection of the experimental plates. Thus the $n = 0$ mode determines the dominant (average) contribution to the amplitude of these short wavelength modes; in this sense we can say the $n = 0$ mode describes the dominant short wavelength behavior in the bubble ensemble. According to this analysis, we regard Fourier modes in the range $0 < n \leq n_{\max}/2$ as long wavelength perturbations.

Bubble height fluctuations, which in the experiments being considered here are reduced by an order of magnitude relative to the mean height, are characterized by the higher mode numbers, $0 < n \leq n_{\max}(t)/2$. In view of

this interpretation, we place this $n = 0$ mode at the position $n_{\max}(t_j)$, after all the other modes. In this manner, we construct modal amplitudes $A(n,t)$ for $0 \leq n \leq n_{\max}(t)/2$ for $t = t_j$, $j = 3, 4, 5, 6$ and for five experiments (#56 and #63 [5] and #104, #105, #114 [54]).

In $Z_{n_{\max}}$, $n_{\max} = 0$, so the convention regarding the $n = 0$ mode is a mathematical identity. But this distinction between $n = 0$ and $n = n_{\max}$ will be important later, when we interpret the $Z_{n_{\max}}$ modes for the purpose of numerical simulation initial conditions, as defining sin and cos modes on the periodic interval $[0, 1]$. See Section4.5. In this case the $n = 0$ mode and the $n = n_{\max}$ mode are distinct.

4.3 A Theoretical Model for Modal Dynamics

We introduce a theoretical model for the dynamics of the modes $A(n,t)$, based on three ideas:

1. Superposition, so that $A(n,t)$, $0 < n < n_{\max}(t)/2$ moves independently of the other modes,

2. Single mode dynamics, so that $A(n,t)$, $0 < n < n_{\max}(t)/2$ propagates with the exponential growth law of the linear dynamics of dispersion relations. In principle, non-linear dynamics for larger amplitudes could be used, but for the experimental data analyzed, $A(n,t)$ is small relative to the modal wavelength.

3. Special dynamics for the dominant short wave modes $A(n_{\max}(t_j))$ based on the bubble merger model [53, 21, 23, 8]. The bubble merger model

propagates short wavelength modes from a previous step, $t = t_{j-1}$, into short wave modes for $t = t_j$. These t_{j-1} modes have a higher mode number, so this propagation is not by superposition within a single mode number. It involves a coupling in the dynamics between distinct short wavelength modes at different times, thus coupling across distinct mode numbers. According to the bubble merger concept, two or more adjacent bubbles at time t_{j-1} combine or are "merged" to produce a larger bubble, with a smaller mode number, but still the short wave mode for the new time t_j.

The first, and primary, purpose of the modal dynamics model is to run backward in time and reconstruct the unobserved long wavelength modal amplitudes $A(n, t_0)$ of the initial data. This purpose does not make use of the short wavelength modes, and so it depends of ideas 1 and 2 above only.

The second purpose of the model is to predict observed data $A(n, t_j)$ from adjacent times $t_{j\pm1}$. This exercise generates errors, which we analyze statistically to ascertain the quality or reliability of the reconstructed $t = t_0$ data. In this way, UQ simulation error bars related to initial condition uncertainty can be assessed. Since we are interested in errors in the predictions of the initial long wavelength modes, this purpose is also served by steps 1 and 2 above only. The third purpose of the theoretical model is to contrast it to a model based on the principle of superposition, in which the motion of each Fourier mode of the bubble interface moves independently of the other modes. Such a model is loosely related to [10]. For the purposes of comparison, we also take some liberties with the bubble merger model [8]. The two models

differ only in their assumptions related to step 3, which is thus crucial for this third purpose.

4.4 Long Wavelength Modes in Initial Data

A self-similar initial spectral power law $A(n)^2 \sim n^{-4}$ for the $t = 0$ amplitudes has been proposed [26, 55, 10]. A similar power law was reported in the initial conditions for the surface of a glass ICF pellet, with higher amplitudes for the smaller wavelengths [10]. We find a power law $A(n)^2 \sim n^{-3.3}$ (mean exponent averaged over five experiments) in the reconstructed $t = 0$ spectra. See Fig. 4.1, top frame. The self-similar power law satisfied by the initial data [54, 5] is not sustained in the third and all later experimental plates. The long wave contribution to the total spectral energy drops from 80% or more initially (when considered over 5 experiments) to less than 0.5% for $t = t_3$ and all later observational times, [28]. See Fig. 4.1, bottom frame and Table 4.1 for this data for experiment #105.

The Z_n amplitudes are used to construct Fourier modes; the Fourier modes determine the initial data. The data as analyzed has amplitude information only and no phase information. Accordingly, we assign random phases for each amplitude. There is no long wavelength data in the y (depth or into plane direction in the figures), and we set all long wavelength amplitudes in this direction to zero. Fourier analysis over $[0, 1]$ differs from that over Z_n, in that there are independent Fourier modes for wave numbers for any value of n, and specifically in the short wave range $n_{\max/2} < n \leq n_{\max}$. In this range we assign random amplitudes with a total spectral weight $A(0, 0)$, for both x

Table 4.1: Experiment #105. Mean spectral exponent for $A^2(n, t_j)$, excluding $n_{\max}(t_j)$ and long wave mode spectral energy (also excluding $n_{\max}$) as a percent of total spectral energy.

Step #	Mean spectral exponent	Long wave spectral energy (%)
t_0	-2.04	99
t_3	-0.18	0.4
t_4	-0.2	0.3
t_5	1	0.2
t_6	–	0.2

and y directions.

4.5 Uncertainty Quantification for Initial Conditions

Here we quantify the errors associated with the modal dynamics and thus with the transfer of data between nearby time steps, as based on the superposition assumption for $0 < n \leq n_{\max}(t_j)/2$. The error estimates in the $t = t_0$ reconstructed initial data are used to establish an uncertainty quantification interval for numerical simulations of the RT growth rate α.

We compare directly observed data to predicted (transferred by modal dynamics) data for 5 experiments, for each of approximately 5 modes, $0 < n \leq n_{\max}/2$. For the comparison of time adjacent experimental plates, we propose a formula

$$\text{error} = |A_{\text{obs}} - A_{\text{pred}}| = aA_{\text{obs}} + b \tag{4.3}$$

to express the discrepancy between observation and prediction. We attribute b to the uncertainty or error in reading bubble height data from scanned images

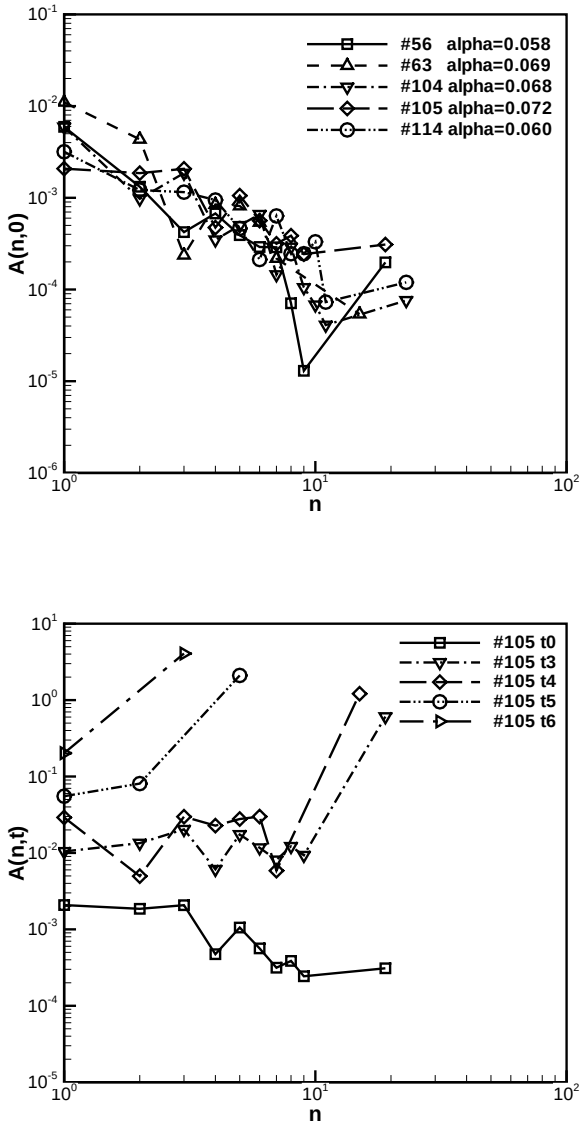

Figure 4.1: Spectral amplitudes $A(n,t)$ vs. wave number n derived from heights of bubble minima. The wave number $n = 0$, which represents the dominant short wavelength mode, is plotted to the right, after all other n values. Top: $t = 0$ data as reconstructed. Bottom: All modes plotted for experiment #105, for all times, labeled as t_j for the j^{th} experimental plate. Data t_0 is the reconstructed initial conditions and the later t_j are as measured from experiment.

of published experimental plates, with an estimated value of 50μ, and we estimate $a = 1.0$. We attribute a to errors in the theoretical model for modal dynamics. The error analysis is illustrated in Fig. 4.2, top frame. In Fig. 4.2, bottom frame, we show a similar scatter plot for the $t = t_0$ data reconstruction. We reconstruct twice, from t_3 and from t_4, and plot the two predictions relative to their mean. In both cases the error bounds defined by (4.3) are drawn in the figure. We see that the error bounds encompass over 95% of the data and thus define 95% confidence intervals for the reconstruction.

We comment that the error bound $a = 1$ is large, and leads to long wavelength perturbations nominal $\pm 100\%$ bracketed by (a) 0 and (b) $2\times$ nominal. Thus choice 0 amounts to pure short wavelength initial perturbations, and the choice 2 allows double the inferred long wavelength initial perturbation plus short wavelength perturbations. The short wavelength spectral amplitude is set to agree with the reconstructed $A(0, 0)$ value. Even with this large bound, the effect on α is $\pm 5\%$. The proper units for b is the same as the errors themselves; these are in microns, and reflect the width (fuzzy edge) of the interface in the experimental plates.

We initialize simulation data with long wavelength perturbations equal to (a) 0, (b) two times the inferred long wavelength initial data. These simulations will give a prediction of α with uncertainty quantification bounds as is related to the initial long wavelength initial conditions. See Table 2.1 and Chapter 5 Fig. 5.1, top frame. In the initialization, we use the Fourier amplitudes of the $Z_{n_{\max}}$ modes to define sin and cos modes on a periodic interval $[0, L]$. The $n_{\max}$ mode and adjacent high wave number modes are replaced by

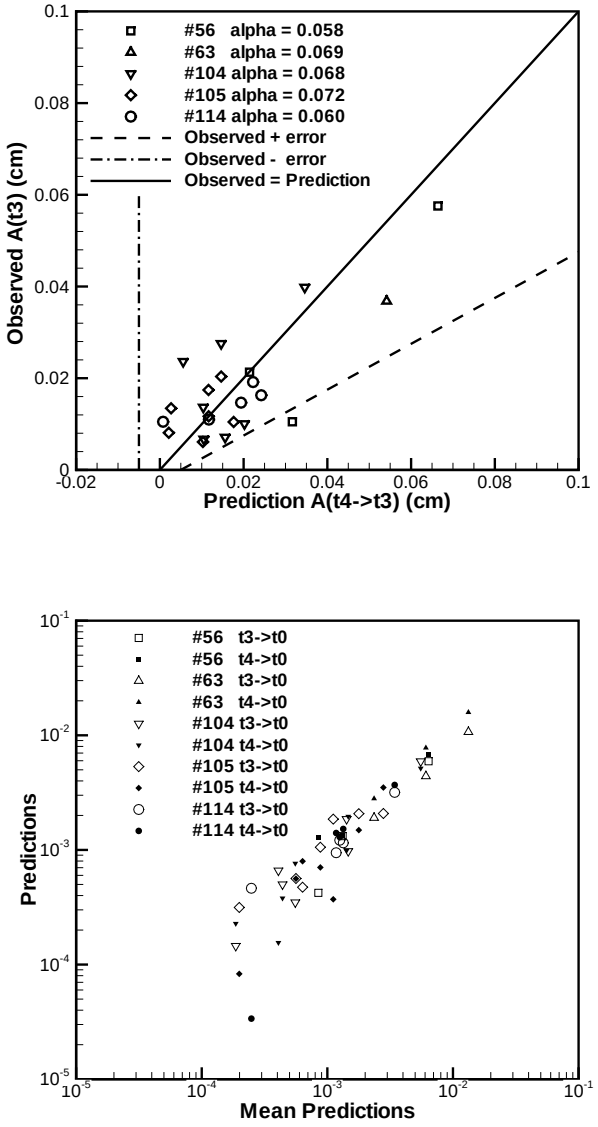

Figure 4.2: Scatter plot data from five experiments with error model bounds for $a = 1.0$ and (top) $b = 50$ microns. In the bottom plot, $b = 2.5$ microns, reduced by a typical propagation factor associated with the transfer of data to $t = t_0$. Top: observed vs. predicted modal amplitudes for $t = t_3$, with the prediction based on $t = t_4$ observations. Bottom: Prediction of $t = t_0$ data, based on $t = t_3$ and $t = t_4$ data, predictions vs. mean of $t = t_3$ and $t = t_4$ predictions.

a wave packet (uniform in k space), spread over the short wavelength interval, having the same total spectral energy.

Chapter 5

Comparison of Bubble Merger and Superposition Models for the $A(n_{\max}(t), t)$ Dynamics

For $n = n_{\max}(t)$, the superposition model replaces item 3 (bubble merger) with superposition, with an enhanced nonlinear single mode velocity about double the single mode velocity itself. Such a doubling of the nonlinear single mode velocity was observed in an analysis of experiments [24] and incorporated into the derivation of the bubble merger models. Thus superposition employs one but not all aspects of the bubble merger dynamics.

The critical difference between the bubble merger and the superposition dynamics defined here lies in the propagation of the shortest wavelength mode, $n = n_{\max}$. Within the dynamics, the key difference is the starting point at each time step for the dynamics.

In the bubble merger model, propagation comes from the shortest wavelength at an earlier time, which has a smaller wavelength and higher mode

number. In other words, smaller bubbles merge to form larger ones at the next time step. Thus (for example) modes at length $\lambda/2$ propagate into modes at length λ.

In the superposition model, the modes with wave number n from an earlier time (when they are not the shortest wavelength) propagate to identical wave number mode n, at later time when they become the shortest wavelength.

To follow the short wavelength dynamics, we refer to Fig. 5.1, bottom frame, in which data points are extracted from Chapter 4 Fig. 4.1, bottom frame. We study the dynamics leading to the short wavelength amplitude $A = A(n_{\max}(t_5), t_5)$ for time $t = t_5$, which in the bubble merger model, comes from $B_1 = A(n_{\max}(t_4), t_4)$ and in the superposition model comes from $B_2 = A(n_{\max}(t_5), t_4)$. These two dynamics require different changes ΔA in the mode amplitudes A, namely ΔA_1 and ΔA_2. Using the evolution relation $\Delta A = v\Delta t$, we see that both dynamics share a common Δt and thus must have different velocities v_1 and v_2. The bubble merger velocity, $v_1 \approx 2\alpha Agt$ is on the order of the maximum velocity present in the bubble region. Since the superposition change in amplitudes ΔA and the resulting required superposition velocity, v_2, is approximately two times larger, we conclude that the superposition model does not describe the experimental data.

In Table 5.1 we compare superposition and bubble merger velocities to the actual bubble front velocity, i.e. to $2\alpha Agt$, for five data points taken from four experiments. Each data point involves predicted dynamics from a time $t = t_j$ to an immediately following time $t = t_{j+1}$. All data propagation pairs from the five experiments with sufficient numbers of bubbles to support this analysis

Table 5.1: Comparison of two model velocities and the exact (experimental) bubble front velocity for five propagation steps between adjacent time levels, drawn from four experiments.

Exp.	prediction steps	mid step times (ms)	$v_{\text{superposition}}$ (cm/ms)	$v_{\text{bubble merger}}$ (cm/ms)	v_{exact} (cm/ms)
#56	$t_3 \rightarrow t_4$	25.6	0.301	0.093	0.133
#63	$t_4 \rightarrow t_5$	29.5	0.404	0.141	0.189
#104	$t_4 \rightarrow t_5$	52.1	0.184	0.071	0.096
#104	$t_5 \rightarrow t_6$	63.1	0.336	0.162	0.117
#105	$t_4 \rightarrow t_5$	48.2	0.201	0.086	0.077

at each of the steps are included in the sample. For all cases, the comparison clearly favors the bubble merger model, while the superposition model fails to explain the experimental data. For two of experiments (#56 and #63) and for predictions made between more distant $t_j \rightarrow t_{j+2}$, etc.) time steps, the same method of analysis occasionally favors the superposition dynamics. For the two experiments (#105 and #114) that are free of long wavelength perturbations, according to the observations or design of the experimentalists or our own directly visible observations (see the discussion of Chapter 1.3), we find that in all cases considered (including prediction over nonadjacent steps) the bubble merger model is favored and the superposition model is inconsistent with the observed data.

Predictions of self-similar mixing and of α [26, 55, 10] have been based on a model for modal dynamics and power law initial modal amplitudes. This modal dynamics model assumes superposition (independence of propagation of distinct Fourier modes). It is thus loosely related to the superposition model discussed here. Since the superposition model discussed here fails to describe

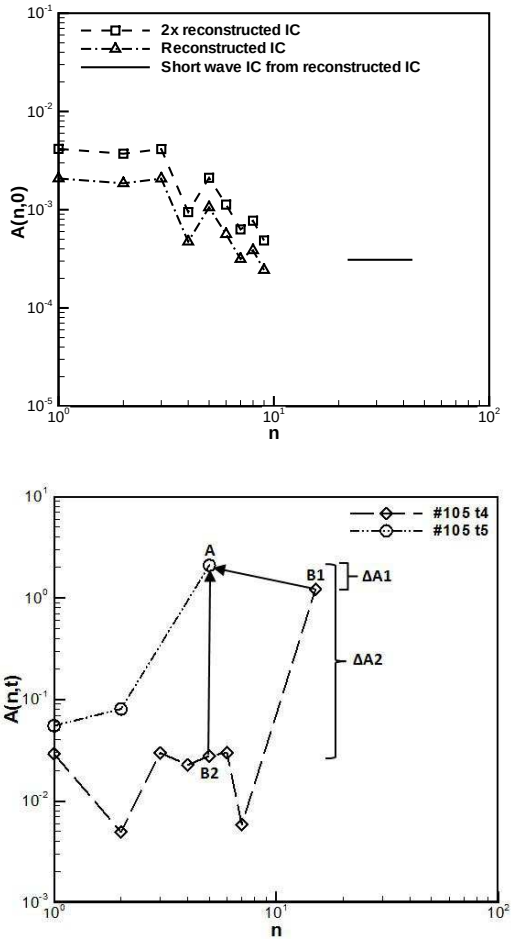

Figure 5.1: Top: Fourier amplitudes based on the periodic interval $[0, L]$. We replace the $n_{\max}$ mode with a wave packet of the same total spectral energy, and we plot the reconstructed long wavelength amplitudes as well as these amplitudes multiplied 2. Cases (a) 0 and (b) 2 times the reconstructed long wave length amplitudes are used to bracket the uncertainty in the reconstruction of the initial conditions. Bottom: Bubble merger and superposition dynamics compared for propagation of point B_1 (bubble merger) or B_2 (superposition) to point A, i with data points taken from Fig. 4.1, bottom frame. The two possible dynamics have a common Δt for different changes ΔA in mode amplitude, and thus different velocities.

the modal dynamics in a manner consistent with experimental data, especially in cases not deliberately agitated or which do not show visible signs of long wave perturbations in the early time steps, we regard predictions based on superposition as problematic. In place of such predictions, we prefer the bubble merger model predictions and the front tracking numerical simulations with detailed fidelity to experimental detail, both of which do agree with experimental data.

Chapter 6

Uncertainty Quantification for Turbulent Mixing Simulations

Uncertainty Quantification (UQ) for fluid mixing depends on the length scales for observation: macro, meso and micro, each with its own UQ requirements. New results are presented for macro and micro observables [30]. For the micro observables, recent theories argue that convergence of numerical simulations in Large Eddy Simulations (LES) should be governed by space-time dependent probability distribution functions (PDFs, in the present content, Young measures) which satisfy the Euler equation. From a single deterministic simulation in the LES, or inertial regime, we extract a PDF by binning results from a space time neighborhood of the convergence point. The binned state values constitute a discrete set of solution values which define an approximate PDF. The convergence of the associated cumulative distribution functions (CDFs) are assessed by standard function space metrics [30, 32].

LES convergence is an asymptotic description of numerical simulations of the inertial, or self-similar, scaling range of a turbulent flow. In the LES

regime, we are not concerned with convergence in a conventional sense. Such mathematical convergence to a classical or weak solution, as $\Delta x \rightarrow 0$, is a property of direct numerical simulations (DNS), i.e. , simulations with all length scales resolved. For practical problems of turbulence, this goal may be unrealistic. Rather, by (LES) convergence, we mean the behavior of numerical solutions in the LES (inertial) regime, as the mesh is refined. In this regime, there is still a type of convergence, but it may be weaker. Rather than convergence to a weak solution, it may be useful or even necessary to consider convergence of PDFs to a measure valued solution (Young measure). The PDFs capture the local fluctuations of the solution, which are an important aspect of the solution in the inertial regime.

The main result is a convergence study for PDFs and CDFs for an RT numerical mesh refinement study. At present meshes, we find CDF but not yet PDF convergence, a minimum sampling size (supercell size) for the stochastic convergence, and suitable norms for the measurement of convergence.

6.1 Mesh Convergence

For most experiments, the initial conditions were not recorded, and the possibility of influence of long wavelength initial perturbations has been a subject of speculation. We have quantified the allowed long wavelength perturbation amplitudes, by an analysis of the recorded early time data [28, 29, 22]. Including an estimate of the uncertainty of this backward extrapolation of data propagated backward to $t = 0$, we estimate the uncertainty in α_b to be $\pm 5\%$ or less, based on simulations which included (I) no initial long wavelength

perturbation and (II) double the reconstructed long wavelength perturbation amplitudes. This range of initial conditions encompasses our estimates in the uncertainty of the reconstruction. See Figure 6.1. [1]

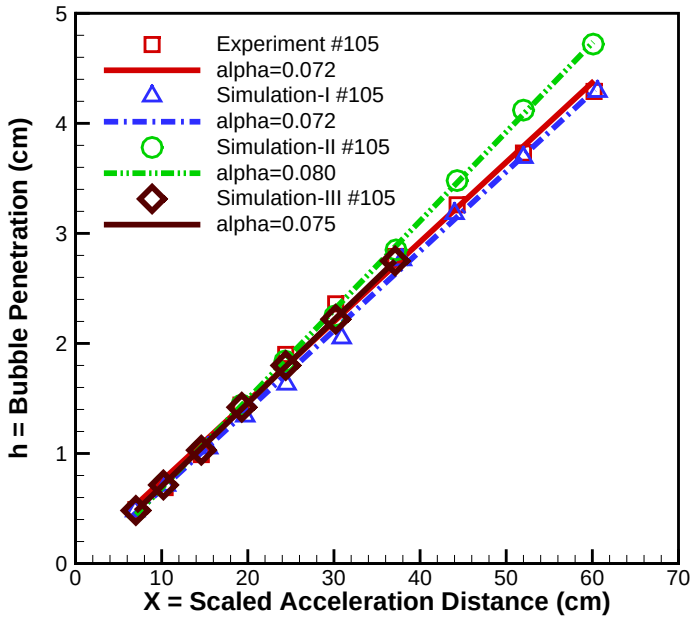

Figure 6.1: Plot of the bubble penetration distance $h_{\rm b}$ vs. a scaled acceleration distance Agt^2. The slope is the mixing growth rate $\alpha_{\rm b}$. We plot the experimental data points and three simulation results, which have (I) $0\times$ and (II) $2\times$ our best reconstruction of the initial long wavelength perturbations, as extrapolated by backward propagation in time from the early time experimental plates. (III) Inferred initial conditions for long wavelength perturbations fully resolved, with a mesh $\Delta x = 111\mu < l_{\rm We} = 130\mu$ where $l_{\rm We}$ is the critical bubble size (predicted by Weber number theory). The simulation III is still in progress.

[1]This research used resources of the Argonne Leadership Computing Facility at Argonne National Laboratory, which is supported by the Office of Science of the U.S. Department of Energy under contract DE-AC02-06CH11357.

6.2 Young Measures

We explain the concept of a Young measure. For a turbulent flow, in the inertial regime, i.e. , for LES simulations of turbulence, the Young measure description of the flow is a much deeper and more useful notion than is a classical weak solution or its numerical approximation. We generalize the notion of test function and of observation, using expectation values $\langle \cdots \rangle$ defined for the integration over the (state) random variables. See also [37].

To start, we suppress the spatial dependence. Thus we have a random system, whose state ξ takes on random values. We introduce a measure space Ω with $\xi \in \Omega$ and a probability measure (unit total measure) $d\nu(\xi)$ on Ω. We denote the result of integrating with respect to ν as $\langle \cdots \rangle$. Then $\langle 1 \rangle = \int_\Omega d\nu(\xi) = 1$.

A measurement is defined by a continuous function f of ξ, and defines a mean or expected value of repeated measurements of f in the random system state $d\nu$, given by the inner product

$$\langle f \rangle = \int_\Omega f(\xi) d\nu(\xi) \ . \tag{6.1}$$

If the expectation yields the value $1/2$, we may conclude that repeated measurements will result in an average value of $1/2$ for f. But we do not know whether the value $1/2$ occurs with each measurement (probability 1), i.e. , perfect mixing with no fluctuations, or whether, at the other extreme, the value 1 occurs with probability $1/2$, that is, no mixing at all and total fluctuations. For further information, we look at moments. The second moment of

the concentration ($f(\xi) = \xi$), useful for chemical reaction kinetics, is

$$\langle f(1-f)\rangle = \int_\Omega f(\xi)(1-f(\xi))d\nu(\xi) \ . \tag{6.2}$$

Eq. (6.2) gives information regarding the spread, or dispersion, of the measure ν. A common normalization of (6.2), is the coefficient of variation for f,

$$\theta = \frac{\langle f(1-f)\rangle}{\langle f\rangle\langle(1-f)\rangle} \ . \tag{6.3}$$

Now we add a spatial and temporal variability to all of the above. The measure $d\nu_{x,t}(\xi)$ now depends on x, t. The added value in allowing such a Young measure as a solution is that the local fluctuations are intrinsically associated with the space time point x, t.

The measurement defined by the stochastic observable $g(x, t, \xi)$ yields the expected value $\langle g(x, t, \cdot)\rangle$ at the space time point x, t. We expect this function of x, t to be a distribution, and so assuming that g is smooth (a test function) in its dependence on x, t, the outcome of the measurement is $\int\langle g\rangle dxdt$. Through this formalism, we can apply differential operators to the state $d\nu$, and as we have a governing PDE, we require $d\nu$ to be a solution of this PDE.

In contrast to multiplication by a test function for a weak solution, the values of the w^* limit test function g multiply probabilities, while the state variable values (density, momentum, concentration), etc., the usual units for the values of the test function, now show up as an argument ξ of g. See Table 6.1.

A natural role for Young measures in a mathematical theory of the Euler

Table 6.1: Comparison of weak solutions and Young measures in terms of test functions

	weak solutions
g values multiply	state variables
g arguments	space, time x, t
integration domain	space-time
example	$g(x,t)$ multiplies
	momentum, energy, concentration
	Young measures
g values multiply	probabilities
g arguments	space, time, x, t; state values ξ
integration domain	space-time; state values
example	$g(x,t,\xi)$ multiplies
	probability

equation and its relation to the Kolmogorov turbulence theory is discussed in [7] and references cited there. In this reference, we assume bounds from Kolmogorov theory, which serve as a type of Sobelov inequality for the approximations, and derive strong convergence for solutions of the incompressible Navier-Stokes equations (after passage to a subsequence) to weak solution Euler equation limit, and w^* convergence for passive scalars coupled to the Navier-Stokes velocity field, to an Euler equation Young measure limit.

6.3 Verification for Stochastic (Young Measure) Convergence

The point of view presented here – w^* convergence to a Young measure solution and the coarse grain and sample algorithm to support this type of convergence numerically – needs verification and validation. Preliminary results

in this direction have been established [39, 38, 40, 31]. To discuss convergence of measures, we need to introduce function spaces for convergence. The PDFs themselves are noisy, and convergence of the PDFs directly appear to require difficult levels of mesh resolution. The indefinite integral of the PDFs, namely the probability distribution functions, i.e. , the cumulative distribution functions (CDFs) are introduced for this purpose. These are better behaved and easier to analyze. Standard function space norms on the CDFs can be used, such as L_1 or the Kolmogorov-Smirnov norm L_∞.

We study nonlinear functions of the solution through analysis of second moments. The convergence properties of the second moments depend on the specific variables which enter into the second moment; some converge nicely while others would benefit from a larger statistical ensemble and/or further mesh refinement.

w^* convergence assumes an integration both over the solution state variables and over space and time. It applies to nonlinear functions of the solution. The idea of stochastic convergence is naturally appealing to workers versed in turbulence modeling. It is, however, a point of view which has not had extensive study in the numerical analysis literature, probably due to the requirements or perceived requirements for mesh resolution and the known limits of practicality for DNS simulations of many realistic problems. For this reason, it is of considerable interest to document exactly what is needed to achieve exactly which levels of convergence in exactly which topology.

Here we investigate multiple realizations of these ideas, in that the tradeoffs and issues related to stochastic convergence appear not to be well docu-

mented in the numerical analysis literature. We study integrated convergence through an L_1 norm (relative to integration both in solution state variables and over space-time) for the CDFs. We see that the L_1 norm for spatial integration is preferred to the L_∞ norm, and that this choice for the CDFs appears to be showing convergence. Additional mesh refinement, which will become routine with increasing computing power, will clarify the this property.

We also explore the size of the supercell used to define the PDFs and CDFs. This size defines a tradeoff between enhanced statistical convergence and the quality of the mesh (supercell mesh) resolution. The L_1 norm convergence is enhanced with larger supercells. We study convergence of the PDFs directly. The PDFs do not show convergence in the L_1 norm with present levels of numerical and statistical resolution, but the trend of results suggests that convergence is possible with further mesh refinement.

6.3.1 Convergence of Second Moments

Here we show the convergence under mesh refinement of the second moments for species concentration and velocities, quantities of interest in a miscible Rayleigh-Taylor experiment [54]. Since the quantities we report were not measured experimentally, this study is verification only, not validation.

It is commonly believed (and observed in numerical studies) that fluctuating quantities obey a type of Kolmogorov scaling law [34]. This property, if correct, implies that the fluctuations are represented by a convergent integral, and should be convergence under mesh refinement. Thus the convergence we report here should not be a surprise. Still, the documentation provides

some new information: the level of refinement needed to observe convergent behavior. We generally observe satisfactory convergence through comparison between the medium and finest of the three grids considered here, and unsatisfactory (poor agreement with the refined grid) properties for the coarsest grid. The limits at late time encounter a varying loss of statistical resolution due to the diminished number of statistically independent degrees of freedom at late time. The three grids have a size 520 to 130 microns (4 to 8 to 16 cells per elementary initial wavelength). Of these, we have generally used the medium grid in our previous simulations, while the coarse grid is commonly favored in RT studies [11]. All second moments reported here represent mid plane values, i.e. a slice $z = \text{const}$ from the center of the mixing zone with t fized, and are averaged over all x, y values.

The second moments of concentration, normalized to define the molecular mixing correlation $\theta = \langle f(1-f)\rangle / \langle f\rangle\langle 1-f\rangle$, were studied experimentally (distinct experiments, not reviewed here). Our value for $\theta \approx 0.8$ is consistent with values obtained numerically in related problems by others [44, 45]. Fig. 6.2 displays numerical results for convergence of θ which model experiment [54], #112, with the three grids.

We study the turbulent correlations of density with the z component of the velocity, u_z, in Fig. 6.3. This correlation is related to gradient diffusion models for subscale turbulence models.

Conventionally, velocity fluctuations are studied using mass weighted av-

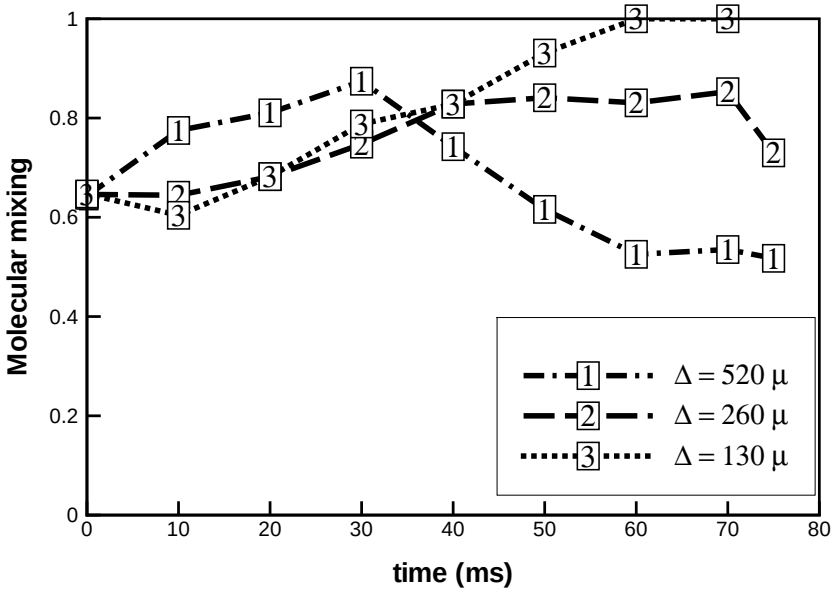

Figure 6.2: Plot of θ vs. time for a numerical simulation of the experiment [54] #112. Three grid levels shown: $\Delta x = 520, 260, 130\mu$. The data has been collected at the mid plane value of z, with an average over all of x, y.

erages, $\widetilde{v} = \langle \rho v \rangle / \overline{\rho}$, and as such serve to define the Reynolds stress

$$R = \langle \widetilde{vv} \rangle - \frac{\langle \widetilde{\rho v} \widetilde{v} \rangle}{\overline{\rho}} \ . \tag{6.4}$$

In Fig. 6.5 we display the simulated Reynolds stress values for [54] experiment #112. The convergence properties for R_{zz} appear to be satisfactory (Fig. 6.5, top). The medium and fine grid display a reasonable level of agreement, while the coarse grid shows a significant discrepancy to the fine grid.

A sensitive comparison is that of R_{xx} to R_{yy}, see Fig. 6.5, bottom frame.

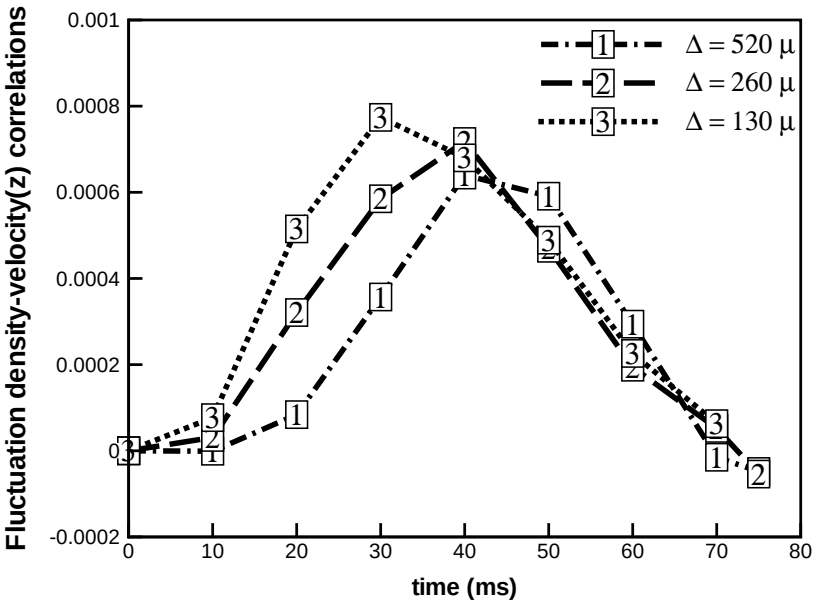

Figure 6.3: Plot of $\overline{\rho' u_z'}$ vs. time. Data from the Z midplane, averaged over all of x, y.

These quantities should be (statistically) identical, so that the solid and dashed curves of the same mesh level family should coincide. This property holds at early but not late time, with the period of agreement increasing under mesh resolution. Moreover, the three curve families should show convergence under mesh refinement, a property which is observed at least up to the time for coincidence of R_{xx} and R_{yy}. The difficulty in the convergence of these quantities appears to be related to the inherently small size of the correlations relative to the statistical noise present in their evaluation and to the loss of statistical significance at late time. As the solution progresses, the correlation length increases, an inherent feature of RT mixing. See the v_z gray scale plot

at $t = 50$ in Fig. 6.6, right frame. Thus at late time, the statistical averaging to define R is drawn from a reduced number of independent degrees of freedom, introducing small sample effects into these components of R at late time.

Similar behavior is observed for R_{xz} and R_{yz}, see Fig. 6.4. Due to the rotational symmetry of the statistical formulation, in the case of an infinite x, y domain, these components should be zero, and any non-zero value is a finite size effect in the statistical sampling. There is satisfactory agreement with these two quantities between each other and with zero, up to a time which depends on the mesh. Because the quantities are sensitive to the sign of v_z statistically, they have enhanced randomness and decreased convergence properties relative to R_{xx} and R_{yy}; they possibly also show small sample size effects at late time.

6.3.2 Convergence of PDFs and CDFs

To define w^* convergence, we need to partition the simulation resolution into resources assigned to the conflicting objectives of spatial resolution and statistical resolution. We consider again the midplane $z = \text{const}$ and $t = \text{const}$, and partition the x, y plane into supercells. We consider several values for the supercell grid, but show detailed results for an 8×2 supercell grid. Here the coarsest grid has for each supercell a resolution 9×6 with a z resolution of a single cell. For the medium and fine grids, the supercell partition is unchanged, but the number of cells in each direction increases by factors of 2 and 4.

For each supercell, we bin the concentration values into 5 bins, and count the number of values lying in each bin, to obtain a probability. In principle,

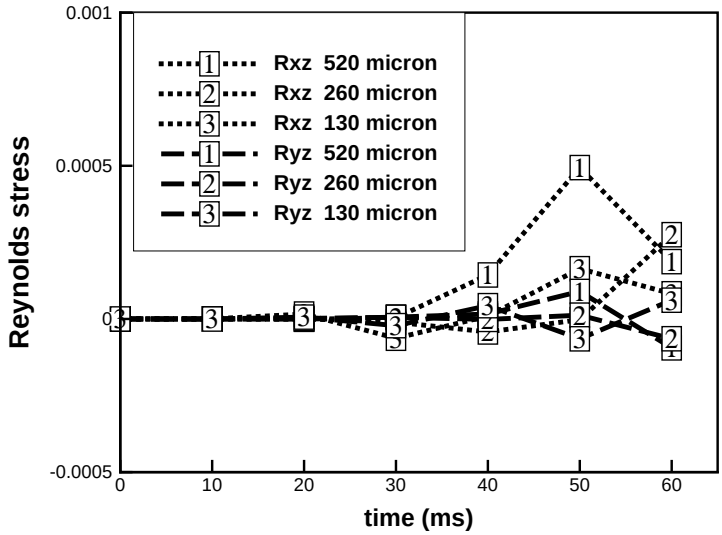

Figure 6.4: Plot of Reynolds stress R_{xz}, R_{yz} vs. time. Plotting time is restricted to a maximum of $t = 60$ as discussed in the text.

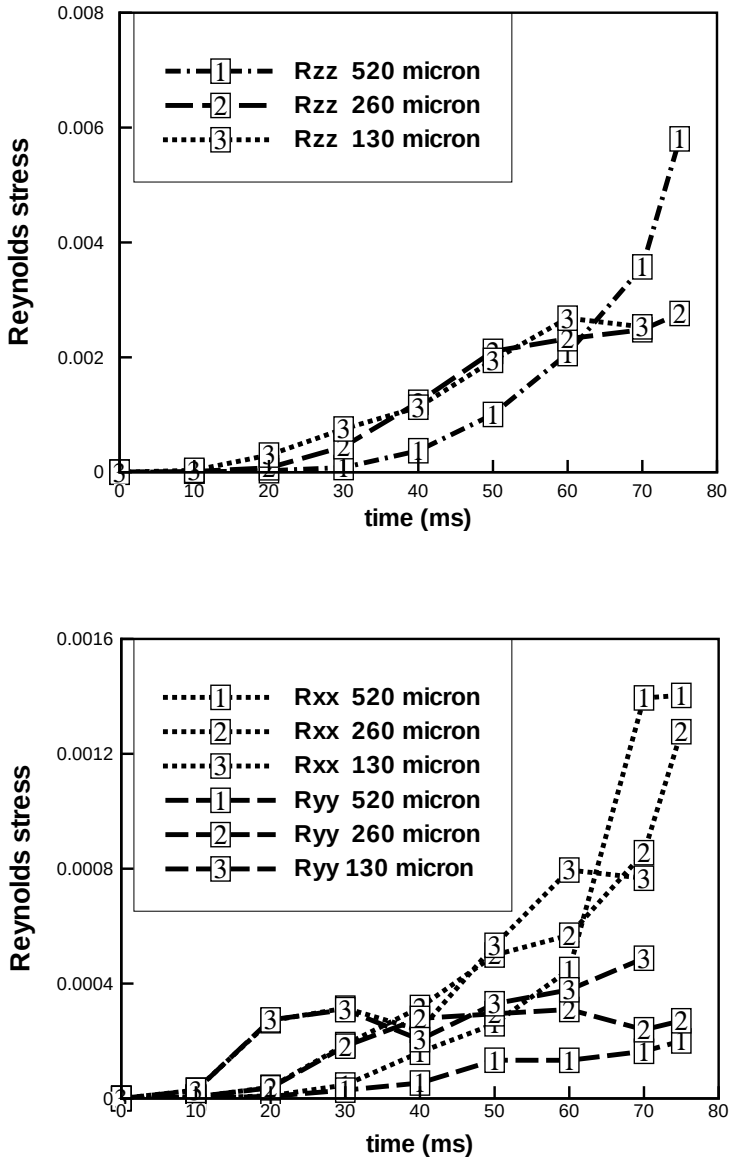

Figure 6.5: Plot of Reynolds stress R_{zz} (top) and R_{xx}, R_{yy} (bottom) vs. time.

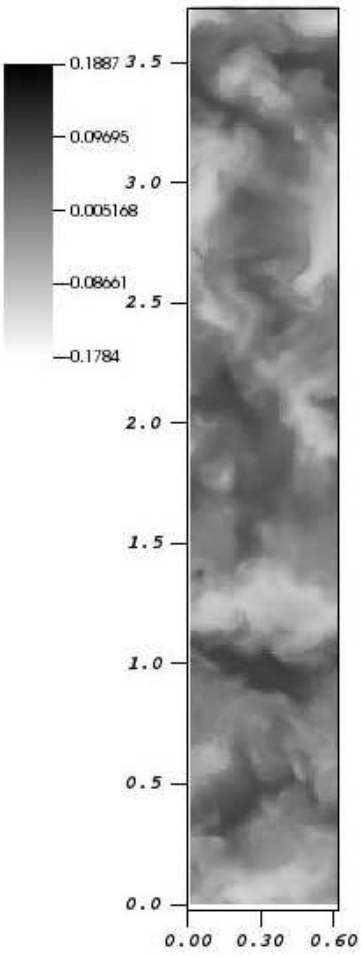

Figure 6.6: Plot of v_z (fine grid, $t = 50$) in the midplane.

the number of bins is another parameter in the analysis, variations in which are not explored here. The result of this exercise is an 8×2 array of PDFs, each represented in the form of a bar graph. The array is a graphical presentation of the Young measure at the fixed z, t value. See Fig. 6.7, 6.8. From this array of PDFs, we can observe some level of coherence or continuity in the spatial arrangement of the PDFs, in that the central supercells have a strong heavy fluid concentration, while near the top and bottom, there is more of a mixed cell concentration.

Next we study mesh convergence of this 8×2 array of PDFs and CDFs. At the late time for the fine grid, we compare the PDFs and CDFs on the coarse to fine and medium to fine grids. The comparison is to compute the L_1 norm of the pairwise differences for each of the 8×2 PDFs or CDFs. These differences yield an 8×2 array of norms, i.e. numbers, which is plotted in Fig. 6.10.

The main results, namely the PDF and CDF convergence properties, are presented in Fig. 6.10. This data is further simplified by use of global norms. With an L_1 norm of the differences of the PDFs or CDFs for concentrations in each supercell, we consider both the L_1 and L_∞ norms relative to x, y variables. With the convergence properties thus reduced to a single number, we next explore the consequence of varying the definitions used for convergence. These are (a) the mesh, (b) PDF vs. CDF, (c) L_1 vs. L_∞ for a spatial norm and (d) the size of the supercell used to define the statistical PDF. See Table 6.2.

We see a convergence trend in all cases under mesh refinement, but useful results for current meshes are limited to CDF convergence. Generally L_1

Table 6.2: Summary norm comparison of convergence for heavy fluid concentration PDFs and CDFs at fixed values of z, t. In each supercell, an L_1 norm is applied to the difference of the PDFs or CDFs; this x, y dependent set of norms is measured by the L_1 or L_∞ norm. The larger supercell sizes, the last four columns of the table, cover the entire y domain. In this case, the space-time localization of the PDFs/CDFs are in x, z, t only. We observe convergence for CDFs; while the PDF error is decreasing, further refinement will be needed for usefully converged PDF errors. We see that a coarsening of the supercell resolution (increase of the supercell size) to 18×12 coarse grid cells per supercell is needed to obtain single digit convergence errors.

coarse grid supercell size	$9 \times 6 \times 1$		$18 \times 12 \times 1$	
mesh comparison	L_1 norm	L_∞ norm	L_1 norm	L_∞ norm
CDFs: coarse to fine	0.26	0.98	0.16	0.48
CDFs: medium to fine	0.18	0.54	0.08	0.16
PDFs: coarse to fine	0.93	4.89	0.59	2.40
PDFs: medium to fine	0.64	2.66	0.30	0.82

coarse grid supercell size	$36 \times 12 \times 1$	
mesh comparison	L_1 norm	L_∞ norm
CDFs: coarse to fine	0.15	0.39
CDFs: medium to fine	0.03	0.10
PDFs: coarse to fine	0.54	1.98
PDFs: medium to fine	0.15	0.52

norms show better convergence, and generally there is a minimum size for the supercell to obtain useful convergence. Since our convergence properties are documented for the medium grid (through comparison to the fine grid), we can speculate that the errors at the fine grid level would be smaller and that some of the above restrictions might be relaxed in this case.

6.3.3 The software tool w^*

A detailed description of this tool will be presented in the dissertation of Ryan Kaufman. Here we report our experience as a user of this software tool, w^* [33], designed to aid in comparison of Young measures and to assess w^* convergence rates. The goal is to compare discrete approximations to Young measures. The Young measures are defined in terms of PDFs and their indefinite integrals, the CDFs. These are discretized relative to space-time and also discretized relative to the solution state variables over which the measure is defined. For the space time discretization, we use a grid, which will normally be a coarsening of some (simulation) grid on which the data is presented. The method is applicable as well to inertial range data of an experimental or observational nature. We refer to the cells of the coarsened grid as supercells. There is also a discretization of the solution state variables. These can be thought of as bins. The number of entries in a bin (the "counts") define an empirical frequency, and a discrete approximation to the Young measure at the supercell location. The degree of discretization of the Young measure, i.e. the bin size, is a convergence issue quite different from conventional grid resolution issues. There is a tradeoff between the loss of information caused by a coarse gridded bin size, as no knowledge of solution values internal to a bin is retained, and the loss of information due to the finite sample size. In view of the latter, the finite data approximation to the bin frequencies, these frequencies will be subject to random errors. Standard statistical tests can evaluate this tradeoff; here we choose a reasonable middle value without further analysis.

In comparing two discrete Young measures, we compare the L_1 norm of the difference of their CDFs. Each CDF is a monotone increasing step function. The location of the steps is determined by the bins into which the data has been organized. There is no requirement that the step locations be identical for the two CDFs being compared. This means that the bins defining the two CDFs need have no relation to one another. We do not impose consistency on the state space discretization. It is also possible to reconstruct piecewise linear or higher order interpolants for the CDFs, which also have no requirement of consistency between the Young measures being compared.

The result of the comparison for CDFs using an L_1 norm on the state space CFD differences defines a function on the supercells. For this purpose, we assume the supercell grids are identical. If one supercell is a strict refinement of the other, comparison is still possible, and with the two choices also faced in grid convergence studies, either to average the finer one onto the coarser, or to inject the coarser into the finer supercell grid.

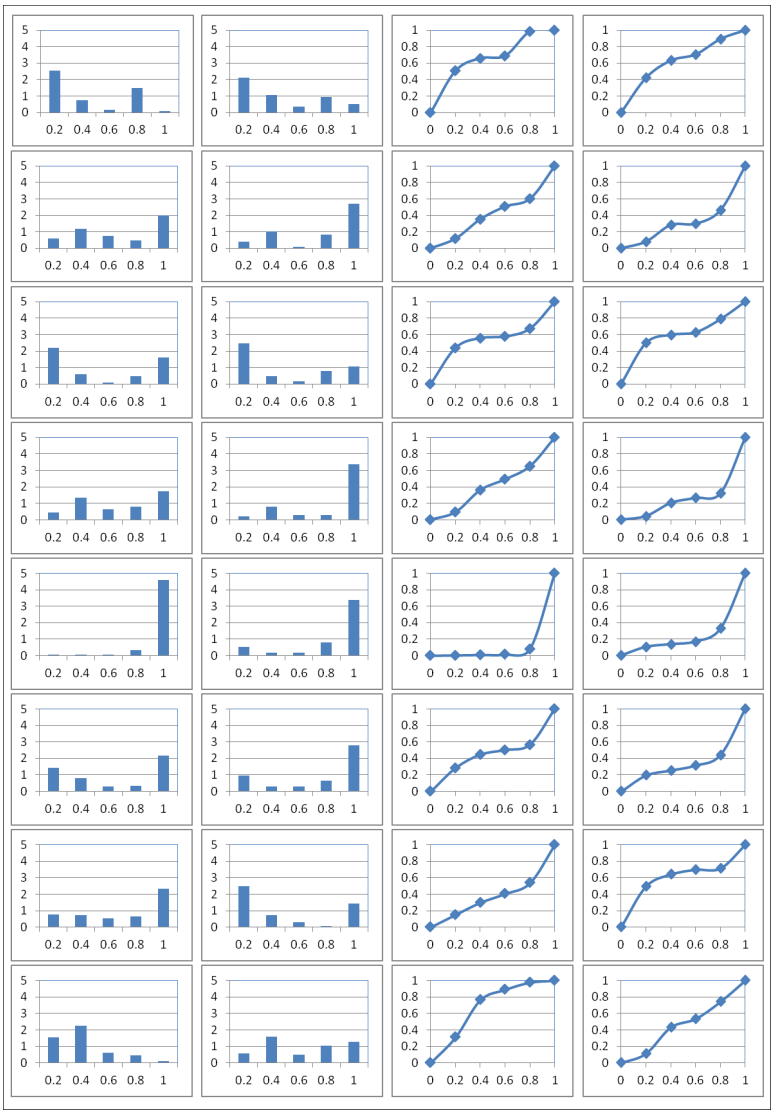

Figure 6.7: Spatial array of heavy fluid concentrations at t = 50, for z in the midplane, as PDFs (bar graphs) and as CDFs (line graphs), Medium grid.

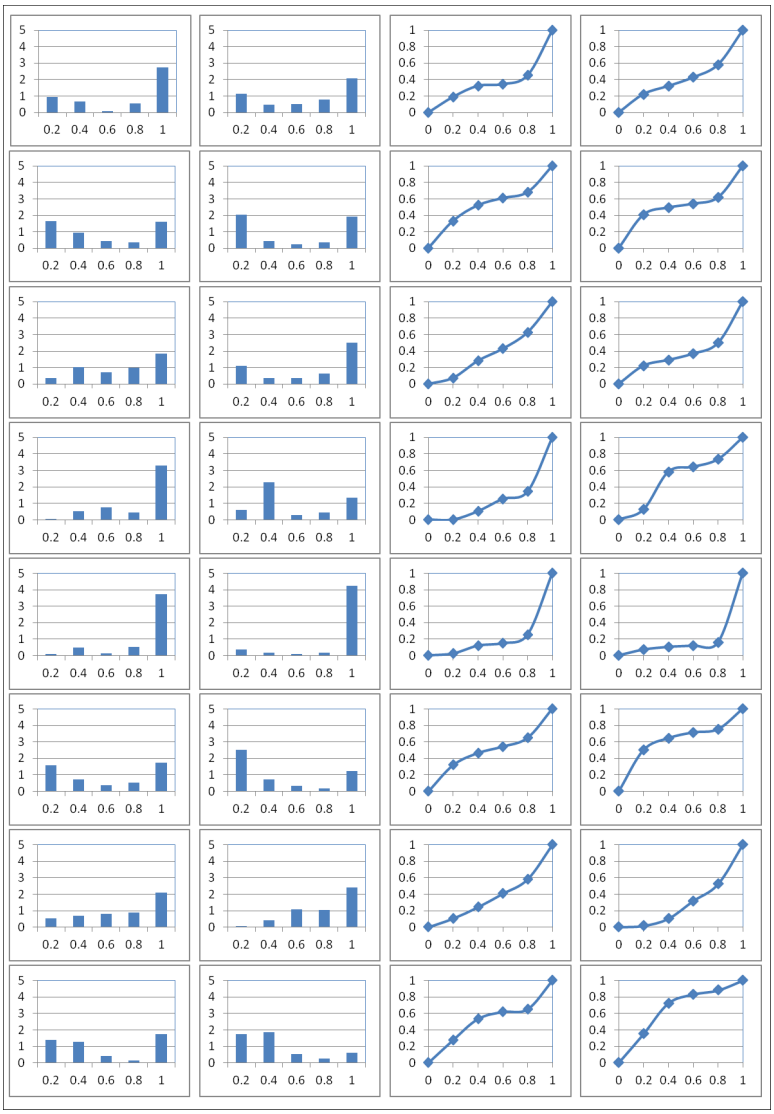

Figure 6.8: Spatial array of heavy fluid concentrations at t = 50, for z in the midplane, as PDFs (bar graphs) and as CDFs (line graphs), Fine Grid.

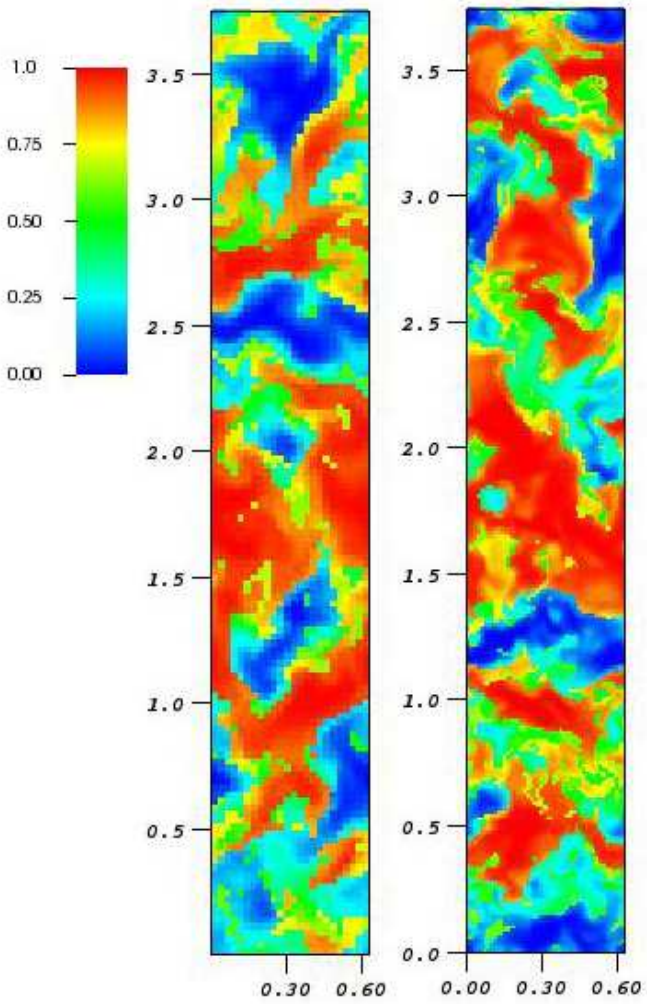

Figure 6.9: Plot of heavy fluid concentration at the midplane, $t = 50$. Medium grid (left). Fine grid (right).

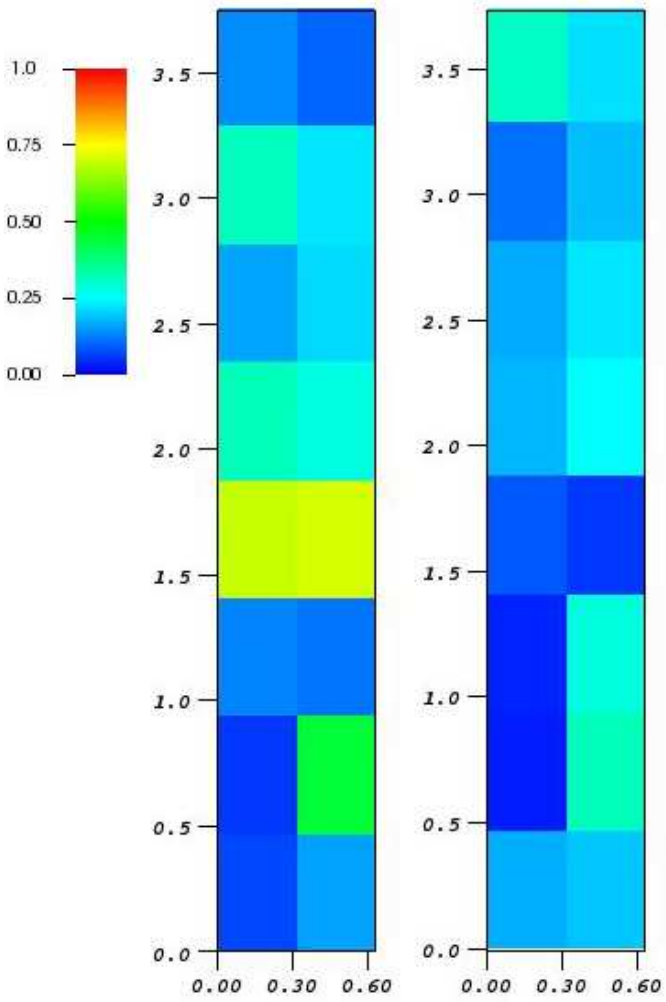

Figure 6.10: Spatial array of L_1 norms of CDF mesh differences for heavy fluid concentrations at the midplane, $t = 50$. Coarse to fine (left). Medium to fine (right).

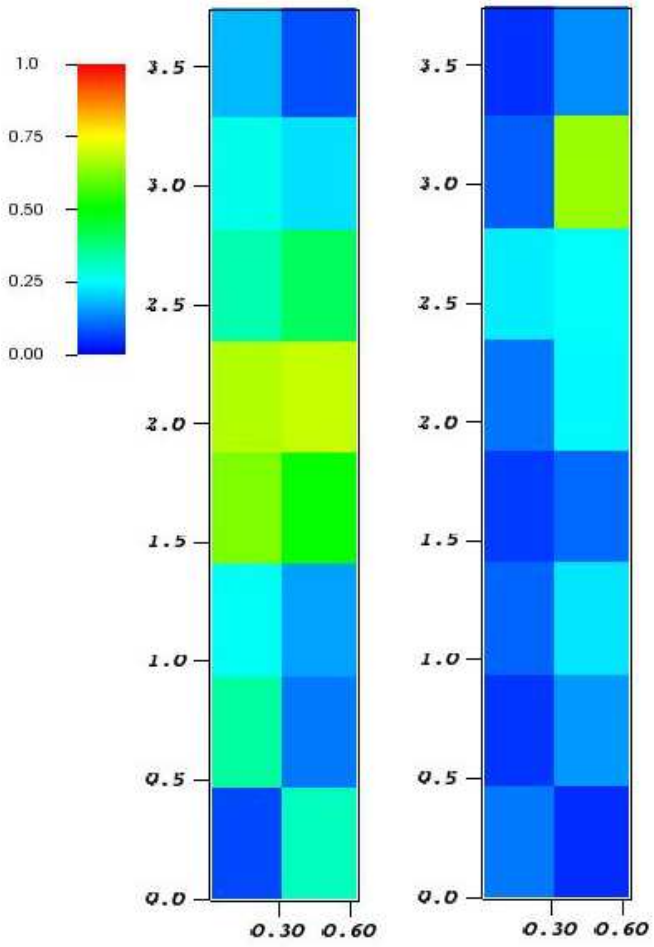

Figure 6.11: Spatial array of L_1 norms of CDF mesh differences for heavy fluid concentrations at the midplane, $t = 70$. Coarse to fine (left). Medium to fine (right).

Chapter 7

Conclusion

We determine that the initial ($t = 0$) long wavelength amplitudes $A(n)$ have a spectral energy $|A^2(n)|$ which satisfies a power law dependence $A^2(n) \sim n^{-3.3}$. Moreover, the long wavelength fraction of the spectral energy (L_2 norm squared) is some 80% of the total spectral energy. We have constrained the uncertainty in initial conditions and have showed a maximum $\pm 5\%$ effect on the growth rate in the uncertainty of the value of α for the Smeeton Youngs experiments. We see that the L_1 norm for spatial integration is preferred to the L_∞ norm, and that this choice for the CDFs appears to be showing convergence. We have established convergence for the CDFs for species concentration in L_1 norm.

We have contributed to an increasing body of validated simulations of the Rayleigh-Taylor mixing rate α across a wide range of explicitly defined experimental situations. We use a compressible code applicable to a variety of compressible turbulent mixing problems. We have addressed one concern regarding these simulations, namely the role of long wavelength perturbations

in the initial conditions. Our simulation results are in disagreement with the claim that long wavelength initial perturbations can affect the αs of presently performed experiments by factors of 2 or 3.

The success of these simulations is based on two principles: careful modeling of all physical detail in the experiments, and the use of an effective, high resolution numerical algorithm. Because α is not universal, it is sensitive to both the modeling issues and the algorithmic issues. Regarding the latter, the essential features of our algorithmic strategy are twofold: tracking to control numerical mass diffusion (sharp interfaces or steep gradients) and LES with dynamic subgrid models to account for the effects of the unresolved scales on the resolved ones. A future issue is to determine the degree to which the present results are partially achieved as the quality of these innovations are partially adopted, as well as to find alternate numerical strategies which duplicate or improve on these results.

Bibliography

[1] AIAA-G-077-1988. *Guide for the Verification and Validation of Computational Fluid Dynamics Simulations*. American Institute of Aeronautics and Astronautics, Reston, VA, 1988.

[2] U. Alon, D. Shvarts, and D. Mukard. Scale-invariant regime in Rayleigh-Taylor bubble-front dynamics. *Phys. Rev. E*, 48:1008–1014, 1993.

[3] A. Banerjee and M. J. Andrews. 3D simulations to investigate initial condition effects on the growth rate of Rayleigh-Taylor mixing. *Int. J. Heat and Mass Transfer*, 52:3906–3917, 2009.

[4] W. Bo, X. Liu, J. Glimm, and X. Li. A robust front tracking method: Verification and application to simulation of the primary breakup of a liquid jet. *SIAM J. Sci. Comput.*, 33:1505–1524, 2011.

[5] K. D. Burrows, V. S. Smeeton, and D. L. Youngs. Experimental investigation of turbulent mixing by Rayleigh-Taylor instability, II. AWE Report Number 0 22/84, 1984.

[6] S. Chandrasekhar. *Hydrodynamic and Hydromagnetic Stability*. Oxford University Press, Oxford, 1961.

[7] G.-Q. Chen and J. Glimm. Kolmogorov's theory of turbulence and inviscid limit of the Navier-Stokes equations in R^3. *Commun. Math. Phys.*, 310:267–283, 2012.

[8] B. Cheng, J. Glimm, and D. H. Sharp. A 3-D RNG bubble merger model for Rayleigh-Taylor mixing. *Chaos*, 12:267–274, 2002.

[9] P. Colella. A direct Eulerian MUSCL scheme for gas dynamics. *SIAM J. Sci. Comput.*, 6(1):104–117, 1985.

[10] G. Dimonte. Dependence of Rayleigh-Taylor instability on initial perturbations. *Phys. Rev. E*, 69:056305–1–056305–14, 2004.

[11] G. Dimonte, D. L. Youngs, A. Dimits, S. Weber, M. Marinak, S. Wunsch, C. Garsi, A. Robinson, M. Andrews, P. Ramaprabhu, A. C. Calder, B. Fryxell, J. Bielle, L. Dursi, P. MacNiece, K. Olson, P. Ricker, R. Rosner, F. Timmes, H. Tubo, Y.-N. Young, and M. Zingale. A comparative study of the turbulent Rayleigh-Taylor instability using high-resolution three-dimensional numerical simulations: The Alpha-Group collaboration. *Phys. Fluids*, 16:1668–1693, 2004.

[12] Jian Du, Brian Fix, James Glimm, Xicheng Jia, Xiaolin Li, Yunhua Li, and Lingling Wu. A simple package for front tracking. *J. Comput. Phys.*, 213:613–628, 2006.

[13] E. George, J. Glimm, X.-L. Li, Y.-H. Li, and X.-F. Liu. The influence of scale-breaking phenomena on turbulent mixing rates. *Phys. Rev. E*, 73:016304, 2006.

[14] E. George, J. Glimm, X.-L. Li, A. Marchese, and Z.-L. Xu. A comparison of experimental, theoretical, and numerical simulation Rayleigh-Taylor mixing rates. *Proc. National Academy of Sci.*, 99:2587–2592, 2002.

[15] M. Germano, U. Piomelli, P. Moin, and W. H. Cabot. A dynamic subgrid scale eddy viscosity model. *Phys. Fluids A*, 3:1760–1765, 1991.

[16] J. Glimm, J. W. Grove, X.-L. Li, K.-M. Shyue, Q. Zhang, and Y. Zeng. Three dimensional front tracking. *SIAM J. Sci. Comput.*, 19:703–727, 1998.

[17] J. Glimm, J. W. Grove, X.-L. Li, and D. C. Tan. Robust computational algorithms for dynamic interface tracking in three dimensions. *SIAM J. Sci. Comput.*, 21:2240–2256, 2000.

[18] J. Glimm, J. W. Grove, W. B. Lindquist, O. McBryan, and G. Tryggvason. The bifurcation of tracked scalar waves. *SIAM J. Sci. Comput.*, 9:61–79, 1988.

[19] J. Glimm, E. Isaacson, D. Marchesin, and O. McBryan. Front tracking for hyperbolic systems. *Adv. Appl. Math.*, 2:91–119, 1981.

[20] J. Glimm, D. Marchesin, and O. McBryan. A numerical method for two phase flow with an unstable interface. *J. Comput. Phys.*, 39:179–200, 1981.

[21] J. Glimm and D. H. Sharp. Chaotic mixing as a renormalization group fixed point. *Phys. Rev. Lett.*, 64:2137–2139, 1990.

[22] J. Glimm, D. H. Sharp, T. Kaman, and H. Lim. New directions for Rayleigh-Taylor mixing. *Phil. Trans. Royal Soc. A: Turbulent mixing and beyond*, 2012. in press. Los Alamos National Laboratory Preprint LA-UR 11-00423 and Stony Brook University Preprint SUNYSB-AMS-11-01.

[23] J. Glimm, D. H. Sharp, and Q. Zhang. The renormalization group dynamics of chaotic mixing of unstable interfaces. *Phys. Fluids A*, 3:1333–1335, 1991.

[24] J. Glimm and X.-Li. On the validation of the Sharp-Wheeler bubble merger model from experimental and computational data. *Phys. Fluids*, 31:2077–2085, 1988.

[25] J. Hecht, U. Alon, and D. Shvarts. Potential flow models of Rayleigh-Taylor and Richtmyer-Meshkov bubble fronts. *Phys. Fluids*, 6:4019–4030, 1994.

[26] N. A. Inogamov et al. In R. Dautray, editor, *Proceedings of the Third International Workshop on Physics of Compressible Turbulent Mixing*, page 1991, Cesta, France, 1991. Commissariat Energie Atomique.

[27] K. Kadau, T. C. Germann, N. G. Hadjiconstantinou, P. S. Lomdahl, G. Dimonte, B. L. Holian, and B. J. Alder. Nanohydrodynamics simulations: An atomistic view of the Rayleigh-Taylor instability. *Proceedings of the National Academy of Sciences*, 101:5851–5855, 2004.

[28] T. Kaman, J. Glimm, and D. H. Sharp. Initial conditions for turbulent mixing simulations. *Condensed Matter Physics*, 13:43401, 2010. Stony Brook University Preprint number SUNYSB-AMS-10-03 and Los Alamos National Laboratory Preprint number LA-UR 10-03424.

[29] T. Kaman, J. Glimm, and D. H. Sharp. Uncertainty quantification for turbulent mixing simulation. *5th International Conference of Numerical Modeling of Space Plasma Flows (ASTRONUM 2010)*, 444:21, 2010. Stony Brook University Preprint number SUNYSB-AMS-10-04. Los Alamos National Laboratory preprint LA-UR 11-00422.

[30] T. Kaman, R. Kaufman, J. Glimm, and D. H. Sharp. Uncertainty quantification for turbulent mixing flows: Rayleigh-Taylor instability. In A. Dienstfrey and R. Boisvert, editors, *Uncertainty Quantification in*

Scientific Computing, volume 377 of *IFIP Advances in Information and Communication Technology*, pages 212–225. Springer, 2012. Stony Brook University Preprint number SUNYSB-AMS-11-08.

[31] T. Kaman, H. Lim, Y. Yu, D. Wang, Y. Hu, J.-D. Kim, Y. Li, L. Wu, J. Glimm, X. Jiao, X.-L. Li, and R. Samulyak. A numerical method for the simulation of turbulent mixing and its basis in mathematical theory. In *Lecture Notes on Numerical Methods for Hyperbolic Equations: Theory and Applications: Short Course Book*, pages 105–129. CRC/Balkema, London, 2011. Stony Brook University Preprint SUNYSB-AMS-11-02.

[32] T. Kaman, J. Melvin, P. Rao, R. Kaufman, H. Lim, Y. Yu, J. Glimm, and D. H. Sharp. Recent progress in turbulent mixing. *Physica Scripta*, 2012. In Press. Stony Brook University Preprint number SUNYSB-AMS-11-09. Los Alamos National Laboratory preprint LA-UR 11-06770.

[33] Ryan Kaufman, Tulin Kaman, Yan Yu, and James Glimm. Stochastic convergence and the software tool W*. In *Proceeding Book of International Conference to honour Professor E.F. Toro*. CRC, Taylor and Francis Group, 2012. In Press. Stony Brook University Preprint number SUNYSB-AMS-11-10.

[34] A. N. Kolmogorov. Local structure of turbulence in incompressible viscous fluid for very large Reynolds number. *Doklady Akad. Nauk SSSR*, 32:141, 1941.

[35] H. Lim, J. Iwerks, J. Glimm, and D. H. Sharp. Nonideal Rayleigh-Taylor mixing. *Proc. Nat. Acad. Sci.*, 107(29):12786–12792, 2010. Stony Brook University Preprint SUNYSB-AMS-09-05 and Los Alamos National Laboratory Preprint LA-UR 09-06333.

[36] H. Lim, J. Iwerks, Y. Yu, J. Glimm, and D. H. Sharp. Verification and validation of a method for the simulation of turbulent mixing. *Physica Scripta*, T142:014014, 2010. Stony Brook University Preprint SUNYSB-AMS-09-07 and Los Alamos National Laboratory Preprint LA-UR 09-07240.

[37] H. Lim, T. Kaman, Y. Yu, V. Mahadeo, Y. Xu, H. Zhang, J. Glimm, S. Dutta, D. H. Sharp, and B. Plohr. A mathematical theory for LES convergence. *Acta Mathematica Scientia*, 32:237–258, 2012. Stony Brook University Preprint SUNYSB-AMS-11-07 and Los Alamos National Laboratory Preprint LA-UR 11-05862.

[38] H. Lim, Y. Yu, J. Glimm, X. L. Li, and D. H. Sharp. Subgrid models in turbulent mixing. *Astronomical Society of the Pacific Conference Series*, 406:42, 2008. Stony Brook Preprint SUNYSB-AMS-09-01 and Los Alamos National Laboratory Preprint LA-UR 08-05999.

[39] H. Lim, Y. Yu, J. Glimm, X. L. Li, and D. H. Sharp. Subgrid models for mass and thermal diffusion in turbulent mixing. *Physica Scripta*, T142:014062, 2010. Stony Brook Preprint SUNYSB-AMS-08-07 and Los Alamos National Laboratory Preprint LA-UR 08-07725.

[40] H. Lim, Y. Yu, J. Glimm, and D. H. Sharp. Nearly discontinuous chaotic mixing. *High Energy Density Physics*, 6:223–226, 2010. Stony Brook University Preprint SUNYSB-AMS-09-02 and Los Alamos National Laboratory preprint number LA-UR-09-01364.

[41] X.-F. Liu, E. George, W. Bo, and J. Glimm. Turbulent mixing with physical mass diffusion. *Phys. Rev. E*, 73:056301, 2006.

[42] T. Ma. *Large eddy simulation of variable density flows.* PhD thesis, University of Maryland, 2006.

[43] P. Moin, K. Squires, W. Cabot, and S. Lee. A dynamic subgrid-scale model for compressible turbulence and scalar transport. *Phys. Fluids A*, 3:2746–2757, 1991.

[44] N. Mueschke and O. Schilling. Investigation of Rayleigh-Taylor turbulence and mixing using direct numerical simulation with experimentally measured initial conditions. I. Comparison to experimental data. *Physics of Fluids*, 21:014106 1–19, 2009.

[45] Nicholas Mueschke and Oleg Schilling. Investigation of Rayleigh-Taylor turbulence and mixing using direct numerical simulation with experimentally measured initial conditions. II. Dynamics of transitional flow and mixing statistics. *Physics of Fluids*, 21:014107 1–16, 2009.

[46] Nicholas J. Mueschke. *Experimental and numerical study of molecular mixing dynamics in Rayleigh-Taylor unstable flows.* PhD thesis, Texas A and M University, 2008.

[47] P. Ramaprabhu and M. Andrews. Experimental investigation of Rayleigh-Taylor mixing at small atwood numbers. *J. Fluid Mech.*, 502:233–271, 2004.

[48] K. I. Read. Experimental investigation of turbulent mixing by Rayleigh-Taylor instability. *Physica D*, 12:45–58, 1984.

[49] W. J. Rider and D. B. Kothe. Stretching and tearing interface tracking methods. In *The 12th AIAA CFD Conference*, San Diego, CA, June 20, 1995. AIAA-95-1717.

[50] W. J. Rider and D. B. Kothe. Reconstructing volume tracking. *J. Comput. Phys.*, 141:112–152, 1997.

[51] O. Sabot, L. Erez, U. Alon, D. Oron, I. A. Lewis, G. Erez, G. Ben-Dor, and D. Shvarts. Study of nonlinear evolution of single-mode and two bubble interaction under Richtmyer-Meshkov instability. *Phys. Rev. Lett.*, 80:1654–1657, 1998.

[52] D. H. Sharp. An overview of Rayleigh-Taylor instability. *Physica D*, 12:3–18, 1984.

[53] D. H. Sharp and J. A. Wheeler. Late stage of Rayleigh-Taylor instability. Technical report, Institute of Defense Analyses, 1961. Unpublished Technical Report.

[54] V. S. Smeeton and D. L. Youngs. Experimental investigation of turbulent mixing by Rayleigh-Taylor instability (part 3). AWE Report Number 0 35/87, 1987.

[55] D. L. Youngs. Application of MILES to Rayleigh-Taylor and Richtmyer-Meshkov mixing. Technical Report 4102, American Institute of Aeronautics and Astronautics, 2003. Presented at the 16th AIAA Computational Fluid Dynamics Conference.

Appendix A

Parameters for the Simulation of Experiment #105

We are concerned with the experiment #105 of Smeeton-Youngs [54] for the immiscible mixing of Pentane and compressed SF_6. The experimental value of acceleration $g = 16g_0$, with g_0 earth gravity, $g_0 = 0.000981\text{cm/ms}^2$, is used. The experimental Atwood number, $A = 0.897$, is used.

We simulate the full size domain and a domain reduced by a factor of 2 in the x and y directions. The parameters describing the simulations are summarized in Table A.1. The simulation I has no long wavelength perturbations in its initial data, while simulation II has twice the estimate provided below for the long wavelength perturbations. The two simulations bracket the uncertainty in the reconstruction of the initial long wavelength perturbations. Simulation III (in progress) uses exactly the reconstructed initial conditions and a 111μ mesh, fully resolving the relevant Weber length scale for droplet formation for immiscible flow. Here $We = 350\mu$ and $Re = 154K$ are the maximum Weber and Reynolds numbers, based on the bubble mixing length

h as a length scale. l_{We} is the critical bubble size (predicted by Weber number theory) and $\lambda_{\mathrm{K}} = 3.7\mu$ is the Kolmogorov scale. The critical bubble size is computed for light fluid bubbles in an ambient heavy fluid, as is needed for the bubble side $\alpha = \alpha_{\mathrm{b}}$ determination, and makes use of fluid parameters from experiment #105 of Smeeton-Youngs [54]. The critical droplet size for heavy fluid droplets embedded in a light fluid ambient is nearly 10 times smaller for this experiment. The main point in simulation III is that we resolve the Weber scale; $\Delta x = 111 < l_{\mathrm{We}} = 130$.

Table A.1: Parameters for the Simulations of Experiment #105 [54]

Simulation	Domain (cm)	Grid	Δx (μ)
I	$15 \times 5 \times 20$	$336 \times 112 \times 448$	≈ 446
II	$7.5 \times 2.5 \times 20$	$336 \times 112 \times 896$	≈ 223
III	$7.5 \times 2.5 \times 20$	$672 \times 224 \times 1792$	≈ 111

Appendix B

Parameters for the Simulation of Experiment #112

In Chapter 6, we show the convergence of the second moments (See Section 6.3.1 and PDFs and CDFs (See Section 6.3.2) in a miscible Rayleigh-Taylor experiment #112 [54]. We are concerned with experiment #112 of Smeeton-Youngs [54] for the miscible mixing of NaI solution and fresh water. The inference that experiment #112 has no influence from long wavelength initial conditions.

The experimental domain is 15cm $\times$ 2.5cm $\times$ 15cm. According to dispersion theory, based on (i) viscosity, (ii) mass diffusion, and (iii) initial mass diffusion, the wavelength of maximum growth rate is $\lambda = \lambda_{\text{th}} = 0.21$ cm. Accordingly, the initial perturbations are initialized in the range [0.157,0.315] cm, centered about $\lambda = 0.21$ cm. The experimental value of acceleration $g = 39g_0$, with g_0 earth gravity, $g_0 = 0.000981\text{cm/ms}^2$, is used. The experimental Atwood number, $A = 0.308$, is used. The kinematic viscosity is set at $\nu = 1.01\text{E-}5$ cm^2/ms, according to the Handbook of Physics and Chemistry.

The kinematic diffusivity is 1.80E-8 cm^2/ms and the Schmidt number is 560. The thickness of the initial mass diffusion layer is 0.35 cm.

We simulate a domain reduced by a factor of 4. For the quarter sized domain, the parameters describing the simulations of experiment #112 with three grid are summarized in Table B.1. The three grids have a size 520 to 130 microns (4 to 8 to 16 cells per elementary initial wavelength).

Table B.1: Parameters for the Simulation of Experiment #112 [54]

Simulation	Domain (cm)	Grid	Δx (μ)
I	$3.75 \times 0.625 \times 15$	$72 \times 12 \times 288$	$\approx$520
II	$3.75 \times 0.625 \times 15$	$144 \times 24 \times 576$	$\approx$ 260
III	$3.75 \times 0.625 \times 15$	$288 \times 48 \times 1152$	$\approx$ 130